Materials Horizons

ROYAL SOCIETY OF CHEMISTRY

REVIEW

View Article Online
View Journal | View Issue

Cite this: *Mater. Horiz.*, 2021, 8, 102

Design strategies for ceria nanomaterials: untangling key mechanistic concepts†

Yuwen Xu, * Sajjad S. Mofarah, Rashid Mehmood, Claudio Cazorla, Pramod Koshy and Charles C. Sorrell *

The morphologies of ceria nanocrystals play an essential role in determining their redox and catalytic performances in many applications, yet the effects of synthesis variables on the formation of ceria nanoparticles of different morphologies and their related growth mechanisms have not been systematised. The design of these morphologies is underpinned by a range of fundamental parameters, including crystallography, optical mineralogy, the stabilities of exposed crystallographic planes, CeO_{2-x} stoichiometry, phase equilibria, thermodynamics, defect equilibria, and the crystal growth mechanisms. These features are formalised and the key analytical methods used for analysing defects, particularly the critical oxygen vacancies, are surveyed, with the aim of providing a source of design parameters for the synthesis of nanocrystals, specifically CeO_{2-x}. However, the most important aspect in the design of CeO_{2-x} nanocrystals is an understanding of the roles of the main variables used for synthesis. While there is a substantial body of data on CeO_{2-x} morphologies fabricated using low cerium concentrations ([Ce]) under different experimental conditions, the present work fully maps the effects of the relevant variables on the resultant CeO_{2-x} morphologies in terms of the commonly used raw materials [Ce] (and $[NO_3^-]$ in $Ce(NO_3)_3{\cdot}6H_2O$) as feedstock, [NaOH] as precipitating agent, temperature, and time (as well as the complementary vapour pressure). Through the combination of consideration of the published literature and the generation of key experimental data to fill in the gaps, a complete mechanistic description of the development of the main CeO_{2-x} morphologies is illustrated. Further, the mechanisms of the conversion of nanochains into the two variants of nanorods, square and hexagonal, have been elucidated through crystallographic reasoning. Other key conclusions for the crystal growth process are the critical roles of (1) the formation of $Ce(OH)_4$ crystallite nanochains as the precursors of nanorods and (2) the disassembly of the nanorods into $Ce(OH)_4$ crystallites and NO_3^--assisted reassembly into nanocubes (and nanospheres) as an unrecognised intermediate stage of crystal growth.

Received 19th April 2020,
Accepted 26th August 2020

DOI: 10.1039/d0mh00654h

rsc.li/materials-horizons

Introduction

Ceria (CeO_2) is a wide band gap semiconductor of considerable importance through its multifarious uses in catalysis,[1–4] photocatalysis,[5,6] energy storage,[7] energy conversion,[2,8,9] gas sensing,[3] and health.[10] Most of these applications depend on the oxygen storage capacity of what effectively is CeO_{2-x}.[12] It also has therapeutic prospects in biomedicine,[11–13] cancer treatments,[12] and neurodegenerative disorder treatments[13] owing to its controllable and pH-dependent $Ce^{4+} \leftrightarrow Ce^{3+}$ redox switching capability.[14] The oxygen storage and redox capacities of CeO_{2-x} are largely dependent on the type and concentrations of defects, particularly oxygen vacancies, which depend on the particle morphologies and associated exposed crystallographic surfaces.[14–17]

More specifically, CeO_{2-x} has been emerging as a significant functional material, including as catalysts for automotive catalytic convertors (three-way catalysts), steam reforming, water-gas shift reaction, hydrocarbon reforming, dehalogenation, and hydrogenation; as catalyst support; in fuel cells (as electrolyte in solid oxide fuel cells and oxygen permeation membrane in polymer exchange membrane fuel cells); as electrochromic films; as sensors for O_2, NO, and hydrocarbons; and as ultraviolet absorbents.[18–20] Conventionally, it is well known as a glass polishing compound and, more recently, it has been used in both biomedicine as a redox catalyst for cell therapies and in environmental chemistry as a photocatalyst for water and air purification.

Ce metal is present at an average concentration of 66.5 ppm in the earth's crust, making it the 25th most abundant of the 94 naturally occurring elements in the earth's crust and the most abundant of the 15 elements known as *rare earths*, *lanthanides*, or 4*f*.[21] Ce metal was identified first by Jöns Jacob Berzelius and Wilhelm Hisinger in Stockholm in 1803 and was named after

School of Materials Science and Engineering, UNSW Sydney, Australia.
E-mail: yuwen.xu@unswalumni.com, C.Sorrell@unsw.edu.au

† Electronic supplementary information (ESI) available. See DOI: 10.1039/d0mh00654h

the recently discovered asteroid Ceres.[22] Its first technical application was as a minority element in ThO_2-CeO_2 mantles for gaslighting in the 1890s.[23]

The most stable oxide of Ce is CeO_2, which is unique among the rare earths as Ce is the only such element to exhibit a stable 4+ valence.[23] CeO_2 is known as ceria, cerium dioxide, ceric oxide, or its mineral name cerianite. However, since the most stable valence for all other lanthanides (Ln) is 3+, then Ce_2O_3 (cerium sesquioxide, dicerium trioxide, or cerous oxide) is a second highly stable oxide. CeO_2 is produced commercially by beneficiation from bastnäsite (a lanthanide fluoride carbonate rock) and monazite (a lanthanide thorium phosphate mineral).

According to the Web of Science database, the first 20th Century technical paper on CeO_2, which was on CeO_2–ThO_2 catalysts, was published in 1928.[24] The total number of papers published between the second paper on CeO_2 in 1950 (ZrO_2–CeO_2 phase equilibria) and 1979 was only 29; these papers included the first consideration of CeO_2 in solid oxide fuel cells in 1966.[25]

However, continued interest in CeO_2 as an electrolyte for this application led to an increase in the number of publications on CeO_2 to $\sim$8 per year until 1987, at which point the annual publication numbers reached double-digit, as shown in Fig. 1. Since then, the publication rate has increased significantly,

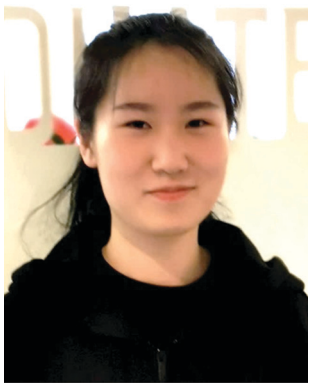

Yuwen Xu

Yuwen Xu received her BEng degree in Materials Science and Engineering (2016) from Northwestern Polytechnical University in China and her MPhil degree in Materials Science and Engineering (2020) from UNSW Sydney in Australia. Her research interests have developed along the lines of ceramic processing and characterisation under the guidance of her colleagues Dr Pramod Koshy, Dr Sajjad S. Mofarah, and Prof Charles C. Sorrell. The present work is based on the experimental work of her MPhil thesis, which focused largely on the examination of the effects of synthesis conditions on the development CeO_2 morphologies and, in particular, the transmission electron microscopy that has facilitated the development of the mechanistic concepts exposed in the present work.

Sajjad S. Mofarah

Sajjad S. Mofarah obtained his PhD in Materials Science and Engineering, UNSW Sydney, in 2020. Following the completion of his PhD, he was appointed as a Research Associate at the same institution, continuing his work on 2D heterojunction materials based on ultrathin metal-based coordination polymers for catalysis and energy storage. He has remained at UNSW Sydney and currently is working as a Research Associate in the cyclic reprocessing of battery materials. His contribution to the present work is based on his expertise in electrochemistry, defect creation and characterisation, aqueous chemistry, and thermodynamics.

Claudio Cazorla

Claudio Cazorla obtained his PhD in Computational Physics from the Polytechnic University of Catalonia (Spain) in 2006. From 2006 to 2010, he worked as a postdoctoral researcher at University College London (United Kingdom) and, in 2010, he moved to the Institute of Materials Science of Barcelona (Spain) as a JAE-DOC Fellow. From 2015 to 2019, Dr Cazorla was an Australian Research Council Future Fellow in the School of Materials Science and Engineering, UNSW Sydney (Australia), where he now is a Senior Lecturer. Dr Cazorla's interests focus on the applications of computational methods for the prediction and understanding of multifunctional materials.

Pramod Koshy

Pramod Koshy received his PhD in Materials Science and Engineering, UNSW Sydney in 2009. This was followed by his engagement as a Research Fellow in the same organisation since then and he has received continuous funding from a range of industries and the Australian Research Council. He has been employed as a Senior Research Fellow since 2017. His primary research foci have been on the development of environmental technologies in waste resource transformation and catalytic material development for air and water purification. His contribution to the present work lies in design and supervision of the experimental program, thermodynamic analyses, and assistance with data interpretation.

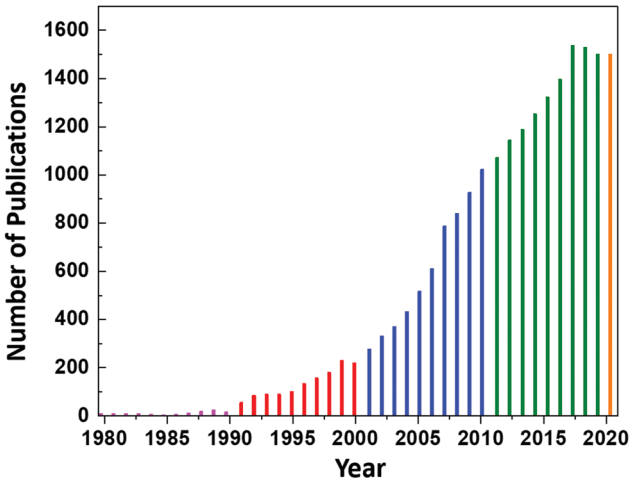

Fig. 1 Annual number of publications according to the search word *ceria* databased by the Web of Science.

reaching a plateau of 1537 publications in 2017 and remaining nearly constant until today (the projection of 1500 publications for 2020 is based on the current publication rate).

CeO_2 crystallography

The crystal structure of CeO_2, drawn to scale according to the eightfold (VIII) coordinated Ce and fourfold (IV) coordinated O radii (the crystal radii are to be used in solids) by Shannon[26] and using the equivalent positions,[27] is shown in Fig. 2. The corresponding crystallographic data for CeO_2 are summarised in Table 1.

The void sizes of the central interstice and the sublattices through which dopants and impurities must pass in order to be dissolved have been calculated because these illustrate the considerable capacity for interstitial solid solubility as two of three of these voids are larger than the ionic radii of the nearly all cations.[26]

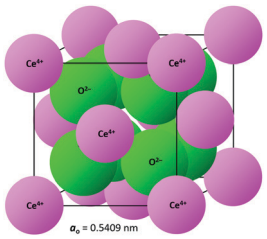

Fig. 2 CeO_2 crystal structure drawn to scale (Ce_{VIII}^{4+} = 0.111 nm, O_{IV}^{2-} = 0.124 nm[26]).

Table 1 Crystallographic data for CeO_2

Category	Details	Information
Crystal system[27]	Cubic	
Prototype structure[27]	CaF_2 (fluorite)	
Space group[27]	International tables	No. 225
	Hermann–Mauguin notation	$Fm\bar{3}m$ or $F4/m\bar{3}2/m$
	Schoenflies notation	O_h^5
	Hall notation	$-F$ 4 2 3
Point group	$m\bar{3}m$	
Pearson symbol	$cF12$	
Strukturbericht designation	$C1$	
Wyckoff sequence	225,*ca*	
Ions per unit cell	12	

Equivalent positions[27]

Cerium sublattice		Oxygen sublattice
Corners	Faces	Corners
0, 0, 0	0, 1/2, 1/2 1/2, 0, 1/2 1/2, 1/2, 0	1/4, 1/4, 1/4 1/4, 3/4, 1/4 1/4, 1/4, 3/4 1/4, 3/4, 3/4 3/4, 1/4, 1/4 3/4, 3/4, 1/4 3/4, 1/4, 3/4 3/4, 3/4, 3/4

Void type	Diameter (nm)	Radius (nm)
Central interstice	0.220	0.110
Ce sublattice face	0.319	0.160
O sublattice face	0.135	0.067

CeO_2 surface stabilities

Although optical mineralogy is useful in describing exposed crystallographic planes, an important complementary approach to materials design is first principles computational methods, typically based on density functional theory (DFT). The stabilities of the different exposed crystallographic planes in CeO_2 can be determined reliably, largely as a result of the ability to solve the relevant quantum mechanical equations without having to make significant approximations of the electronic interactions.[28]

Uncertainties arising from energy band considerations present various challenges to DFT simulations, so several strategies to deal efficiently with the electronic exchange energy and electronic correlations have been developed.[29–32] As a result, a range of DFT

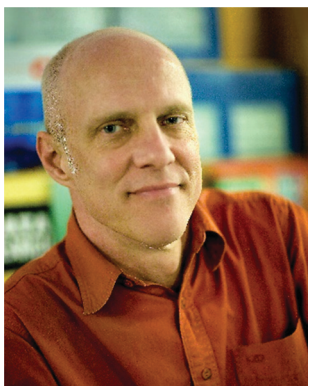

Charles C. Sorrell

Charles C. Sorrell has been the Professor of Ceramic Engineering at UNSW Sydney since 1997. He obtained his BSc degrees in Ceramic Engineering (1977) and Chemistry (1980) from the University of Missouri-Rolla, his MSc degree in Ceramic Science (1980) from the Pennsylvania State University, and his PhD degree in Ceramic Engineering (1987) from the University of New South Wales. His principal research foci have remained in ceramic processing and phase equilibria, which have been applied across many areas. At present, his main work is in catalysis, biomaterials, geopolymers, and waste utilisation. His contribution to the present work draws upon his backgrounds in ceramics, phase equilibria, defect equilibria, crystallography, optical mineralogy, crystal growth, thermodynamics, and kinetics.

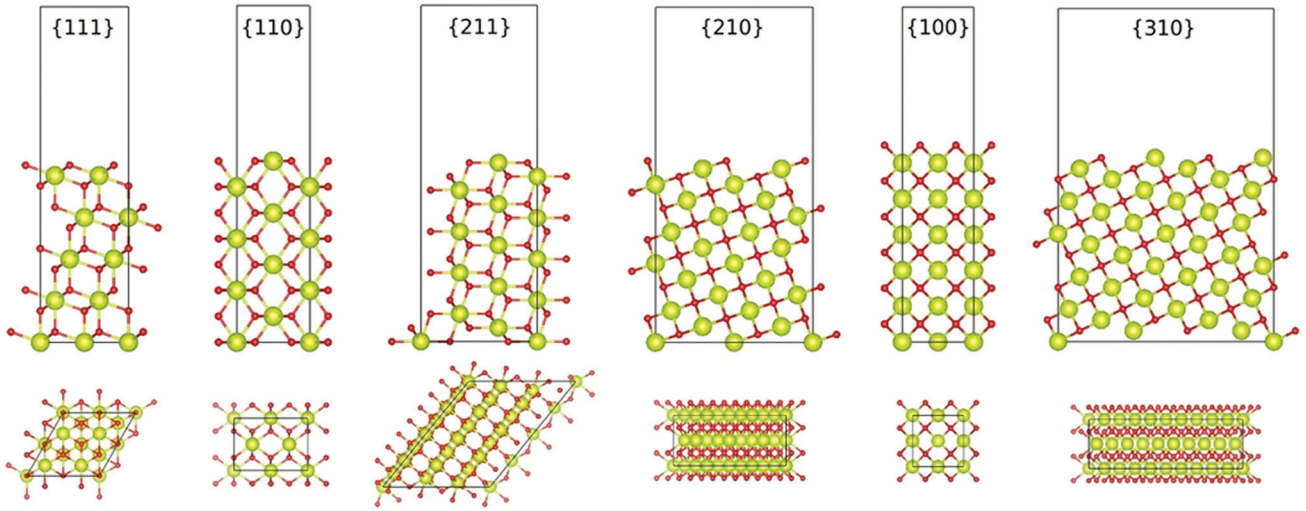

Fig. 3 Ball-and-stick models of various low-index planes in CeO_2 determined by first-principles DFT simulations (illustrating two different views, Ce = yellow spheres, O = red spheres) (authors' unpublished work).

approaches has been applied, the most commonly used of which are (1) local density approximation (LDA),[28,33] (2) generalised gradient approximation (GGA),[28,33,34] (3) Becke 3-parameter Lee–Yang–Parr hybrid functional (B3LYP),[33] and (4) Heyd–Scuseria–Ernzerhof range-separated hybrid functional (HSE).[32] The commonly used LDA and GGA approaches often incorporate a Hubbard-like U term into the relevant quantum Hamiltonian (*e.g.*, LDA+*U* and GGA+*U*) in order to compensate for self-interaction errors.[30] For stoichiometric CeO_2 and nonstoichiometric CeO_{2-x}, the electronic structure is dominated by the Ce 4*f* electronic band at the bottom of the conduction band (CB) and the O 2*p* orbitals at the top of the valence band (VB). The hybridisation of these and other states is assessed by projecting the partial density of states (pDOS) for atomic orbital contributions.[34] This assessment allows the determination of the band gap (E_g) (ESI,† Fig. S1).

Another important capability of DFT is the examination of surfaces as semi-infinite slabs of typically 10–20 atomic layers thickness.[35] This approach can be designed to incorporate different crystallographic orientations, plane polarities, plane ionic terminations, and surface oxygen vacancies. These variables can be introduced and then used to determine, *inter alia*, surface formation energies and adsorption energies. Fig. 3 shows ball-and-stick models of several low-index CeO_2 slabs used to simulate CeO_2 surfaces using DFT. An important outcome of these simulations is the capability of contrasting the stabilities of the different crystallographic planes through the surface formation energies. Table 2 contrasts the stability rankings of the principal low-index planes determined using different approaches, including an early study of molecular mechanics (MM) performed with classical interatomic potentials (IP).[36]

Table 2 Stabilities of low-index crystallographic planes of CeO_2 simulated using different methods

LDA+U[33]	GGA+U[33]	GGA+U[34]	B3LYP[33]	MM/IP[36]	Stability
{111}	{111}	{111}	{111}	{111}	Most
{221}	{221}	{110}	{331}	{110}	
{331}	{331}	{210}	{331}	{211}	
{110}	{110}	{211}	{110}	{100}	
{211}	{311}	{100}	{100}	{210}	
{210}	{210}	{310}	{210}	{310}	
{311}	{100}	—	{211}	—	
{100}	{311)	—	{311}	—	Least

CeO_{2-x} stoichiometry

It is well known that CeO_{2-x} is a nonstoichiometric compound owing to the presence of what effectively are intrinsic oxygen vacancies $\left(V_O^{\bullet\bullet}\right)$.[37–39] As each $V_O^{\bullet\bullet}$ is charge compensated by two $Ce^{4+} \rightarrow Ce^{3+}$ reduction reactions, then an accurate definition of the form of the stoichiometry of CeO_{2-x} is:

$$CeO_{2-x} = Ce_{1-x}{}^{4+}Ce_x{}^{3+}O_{2-\frac{x}{2}}{}^{2-} = Ce_{1-x}{}^{4+}Ce_x{}^{3+}O_{2-\frac{x}{2}}{}^{2-}\square_{\frac{x}{2}}$$

where $\square$ is an oxygen vacancy. This stoichiometry variability is largely responsible for the disagreements in the literature concerning data that are fundamental to CeO_{2-x}, including the lattice parameter (a_o), true density (ρ_{True}), and optical indirect band gap (E_g). These uncertainties are clarified in Fig. 4 by showing the extent of oxygen deficiency (x) as a function of temperature and oxygen partial pressure of Bulfin *et al.*[40] and by using the linear composite data of Schwab *et al.*[41] for the effects of temperature and oxygen deficiency on the lattice parameter of CeO_{2-x}. The latter data have been used to calculate the true density as a function of these two variables. Further, the optical indirect band gap as a function of oxygen deficiency and concentration of oxygen vacancies $\left(\left[V_O^{\bullet\bullet}\right]\right)$ has been determined in the present work (ESI,† Fig. S1) by density functional theory (DFT) simulations based on further refinement of earlier work by the authors.[42] The range of E_g values spans stoichiometric CeO_2 to $CeO_{1.5}$, the latter of which represents the maximal theoretical level of $\left[V_O^{\bullet\bullet}\right]$ of 25%. The equations for these relations are as follows:

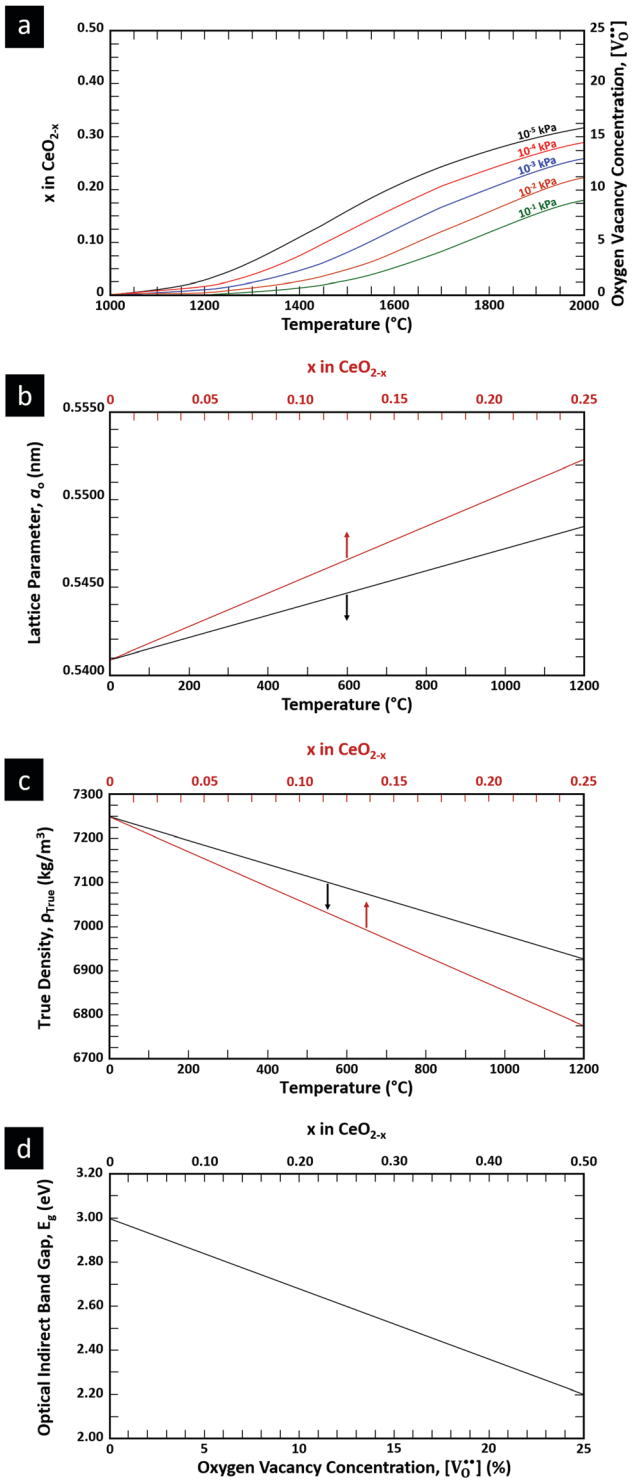

Fig. 4 (a) Effect of temperature on oxygen deficiency,[40] (b) effect of temperature and oxygen deficiency on lattice parameter,[41] (c) effect of temperature and oxygen deficiency on true density (authors' unpublished work), (d) effect of oxygen nonstoichiometry on optical indirect band gap of CeO_{2-x} (authors' unpublished work).

$$a_o = 0.5409 + (6.2708 \times 10^{-6})T$$

$$a_o = 0.5409 + (4.5800 \times 10^{-2})x$$

$$\rho_{True} = 7224.6 - (2.4875 \times 10^{-1})T$$

$$\rho_{True} = 7224.6 - (1.2860 \times 10^{3})x$$

$$E_g = 3.0 - (3.2 \times 10^{-2})\left[V_O^{\bullet\bullet}\right]$$

$$E_g = 3.0 - (1.6)x$$

where: a_o = lattice parameter in nm, ρ_{True} = true density in kg m^{-3}, E_g = optical indirect band gap in eV, T = temperature in °C, x = oxygen deficiency in CeO_{2-x}, $\left[V_O^{\bullet\bullet}\right]$ = oxygen vacancy concentration in %.

Ce–O phase equilibria

The condensed oxide phase equilibria in their entirety are shown in Fig. 5. While these data are based principally on the summary of Okamoto,[43] they have been modified to formalise the five low-stability phases of the suboxide series Ce_nO_{2n-4}, where n = 18–22 in integers. The stoichiometries of these phases as reported (Ce_9O_{16}, $Ce_{19}O_{34}$, Ce_5O_9, $Ce_{31}O_{56}$, $Ce_{11}O_{20}$) scale nearly perfectly to a sequence ($Ce_{18}O_{32}$, $Ce_{19}O_{34}$, $Ce_{20}O_{36}$, $Ce_{21}O_{38}$, $Ce_{22}O_{40}$) that is almost certainly an analogue of a similar series of the nonstoichiometric phases in the Ti–O system. These Magnéli phases[44] are a homologous series of suboxide compositions of the stoichiometry Ti_nO_{2n-1}, where n = 4–10 in integers. They are based on the same TiO_2 crystal structures but differentiated by crystallographic shear in which planar defects are introduced as a function of oxygen deficiency.[45,46] The phase diagram draws attention to a number of potential materials design trajectories for functional materials:

- CeO_2 exhibits solid-state immiscibility at 448–657 °C. These compositions would be likely to generate high concentrations of interfaces, which could serve as sites for $V_O^{\bullet\bullet}$ formation and active sites for catalysis.
- The oxygen deficiency in CeO_{2-x} increases with increasing temperature, reaching a maximum of $CeO_{1.65}$ or $Ce_{0.30}^{4+}Ce_{0.70}^{3+}O_{1.65}^{2-}\square_{0.35}$ (62.25 at% oxygen; $Ce_{0.3775}O_{0.6225}$, x = 0.35;

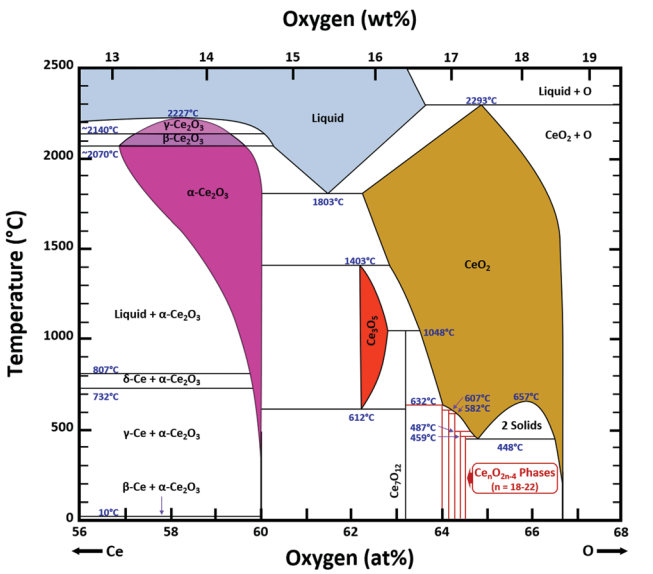

Fig. 5 Ce–O condensed phase diagram based largely on the summary of Okamoto;[43] analogue Ce_nO_{2n-4} suboxide series inferred.

Table 3 Calculated standard-state thermodynamic functions for Ce_nO_{2n-4} (authors' unpublished work)

n	Ce_nO_{2n-4}	ΔG°_{298} (kJ mol^{-1})	ΔH°_{298} (kJ mol^{-1})	ΔS°_{298} (kJ mol^{-1})	C_p (J K^{-1})
18	$Ce_{18}O_{32}$	−934.47	−988.68	72.55	59.48
19	$Ce_{19}O_{34}$	−935.21	−990.51	72.66	59.62
20	$Ce_{20}O_{36}$	−937.71	−992.51	72.83	59.86
21	$Ce_{21}O_{38}$	−939.09	−994.15	72.95	60.02
22	$Ce_{22}O_{40}$	−940.35	−995.64	73.06	60.17

$[V_O^{\bullet\bullet}]$ = 17.5%) at 1803 °C. The use of high temperatures in reducing atmospheres would be likely to increase the $[V_O^{\bullet\bullet}]$.

• Ce_2O_3 has not been investigated to any great degree. Its extent of oxygen deficiency also suggests that it may offer properties that can be engineered similarly to those of CeO_{2-x}.

• Ce_3O_5 does not appear to have been investigated at all. Although its temperature range of stability is limited by eutectoid decomposition at 612 °C and peritectoid decomposition at 1403 °C, it probably can be quenched to room temperature. Its homogeneity range also suggests that it may exhibit interesting properties as a function of stoichiometry variation.

• The Ce_nO_{2n-4} suboxide phases of the inferred analogue of the Magnéli phase series also do not appear to have been investigated. In common with the Magnéli phases, these may exhibit applications as thermoelectrics,[46] conducting oxides,[47] charge storage devices,[48] antiferromagnets,[49] and lubricants.[50]

Finally, the composition of maximal $[V_O^{\bullet\bullet}]$ sometimes is referred to as Ce_2O_3. While this is correct stoichiometrically, the phase diagram demonstrates that this is a misnomer as this phase is a compound distinctly different from CeO_2. Consequently, the correct designation for CeO_{2-x} of maximal $[V_O^{\bullet\bullet}]$ is $CeO_{1.5}$.

Ce–O thermodynamics

The thermodynamic database for the system Ce–O is incomplete. The standard database is that of FactSage 7.3 (ThermFact Inc. & GTT-Technologies, Montreal, Canada), which includes data for CeO_2, Ce_2O_3, Ce_3O_5 (as $Ce_{18}O_{31}$), and Ce_7O_{12} (as Ce_6O_{11}). Owing to the absence of data for the Ce_2O_{2n-4} suboxides, these data have been calculated using the database and software of HSC Chemistry 6.0 (Metso Outotec, Helsinki, Finland). The standard-state data are given in Table 3.

The Gibbs free energies as a function of temperature are shown graphically in Fig. 6; the stability diagram as a function of temperature and oxygen partial pressure (pO_2), calculated using the FactSage 7.3 database,[76] also is given. The equations for the Gibbs free energies of the four principal oxides are as follows:

$$CeO_2 \rightarrow -1031.95 + (0.2051 \cdot \Delta T)$$

$$Ce_2O_3 \rightarrow -857.65 + (0.1370 \cdot \Delta T)$$

$$Ce_3O_5 \rightarrow -947.41 + (0.1708 \cdot \Delta T)$$

$$Ce_7O_{12} \rightarrow -981.62 + (0.1828 \cdot \Delta T)$$

$$Ce_{18}O_{32} \rightarrow -934.47 + (0.1700 \cdot \Delta T)$$

$$Ce_{19}O_{34} \rightarrow -935.21 + (0.1712 \cdot \Delta T)$$

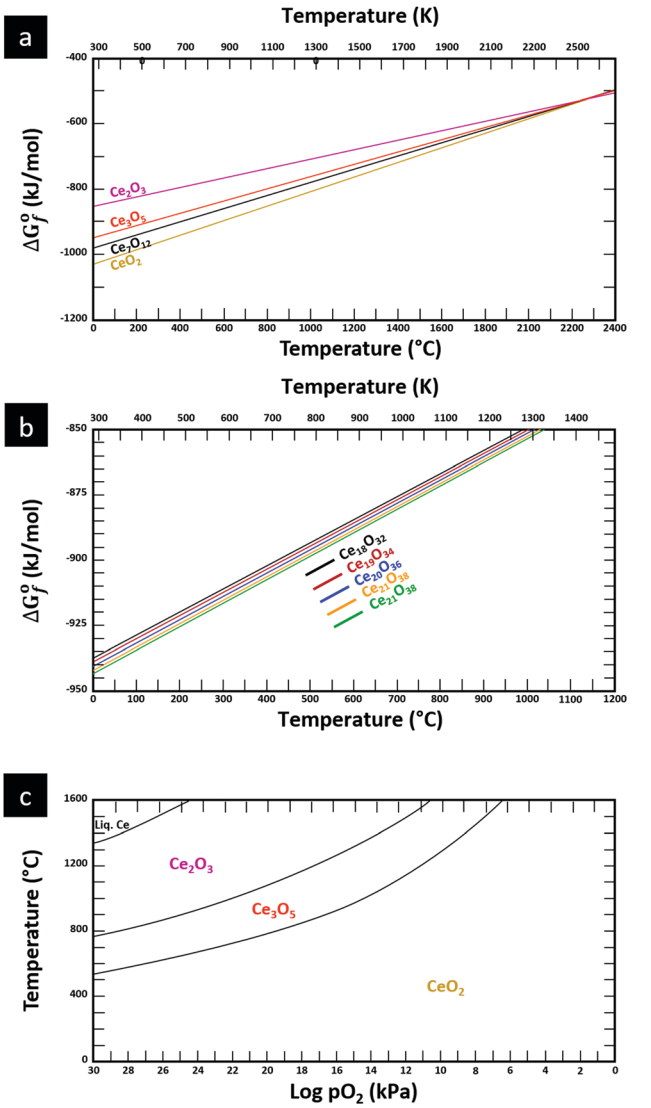

Fig. 6 Thermodynamic data for the system Ce–O: (a) Gibbs free energies for principal oxides based on FactSage 7.3 data, (b) Gibbs free energies for Ce_2O_{2n-4} suboxide series calculated using HSC Chemistry 6.0 data (authors' unpublished work), (c) stability diagram calculated on basis of FactSage 7.3 data.[76]

$$Ce_{20}O_{36} \rightarrow -937.71 + (0.1720 \cdot \Delta T)$$

$$Ce_{21}O_{38} \rightarrow -939.09 + (0.1728 \cdot \Delta T)$$

$$Ce_{22}O_{40} \rightarrow -940.35 + (0.1735 \cdot \Delta T)$$

where ΔT is the temperature difference from 0 °C or 273.15 K.

Ce–O defect equilibria

The synthesis and characterisation of functional materials, such as CeO_{2-x}, are synonymous with point defect engineering. The role of point defects is critical to the performance of these oxides and similar materials and their characterisation is critical to the interpretation of their performance.

However, the defect chemistries of most semiconducting oxides have been reported at high temperatures ($\geq$500 °C) as these are required owing to thermodynamic limitations, which restrict the concentrations and mobilities of charge carriers typically required for the manifestation of the effects as well as detection.[51] In contrast, most reports of the synthesis of CeO_{2-x} typically detail procedures based on precipitation and hydrothermal synthesis, which have been done at considerably lower temperatures ($\leq$200 °C). However, in the case of CeO_{2-x}, the ready $Ce^{4+} \leftrightarrow Ce^{3+}$ redox switching, even at room temperature under the influence of pH change,[6,14] demonstrates that at least some point defects in CeO_{2-x} (*viz.*, surface defects) are mobile at low temperatures.

Defect equilibria in oxides generally are expressed in terms of Kröger–Vink notation.[52] However, a full description of the possible types of defect equilibria using this formalism does not appear to have been presented. Table 4 gives the full range of defect equilibria associated with the five main causation factors:

- Intrinsic: for pure CeO_{2-x}
- Extrinsic: for doped CeO_{2-x}
- Intervalence charge transfer: for doped and codoped CeO_{2-x}
- Multivalence charge transfer: for codoped CeO_{2-x}
- Colour centres: for pure and doped CeO_{2-x}

Since CeO_{2-x} is expressed as $Ce_{1-x}^{4+}Ce_x^{3+}O_{2-\frac{x}{2}}^{2-}\square_{\frac{x}{2}}$ and $Ce^{4+} \rightarrow Ce^{3+}$ reduction is viewed as being ionically charge compensated by $V_O^{\bullet\bullet}$ formation, then this point defect is critical to the synthesis and properties of CeO_{2-x}. The $V_O^{\bullet\bullet}$ formation energy is highly positive and can be varied in the range 1.20–2.25 eV, depending on the crystallite size and exposed facets.[53,54] The most commonly investigated methods of defect formation involve intrinsic or extrinsic considerations. Intrinsic $V_O^{\bullet\bullet}$ typically are generated by heating in vacuum or under reducing atmospheres and extrinsic $V_O^{\bullet\bullet}$ generally are induced by acceptor doping (p-type) with transition or rare earth metals. However, there are other methods by which these and other defects can be introduced:

- Electrochemical defect generation by proton-assisted $V_O^{\bullet\bullet}$ creation (PAOVC) is a novel approach to form high concentrations of volumetric $V_O^{\bullet\bullet}$, where the integration of protons ($H^{\bullet}$) in an aqueous solution can lower significantly the energy (electrical potential) required for the formation of $V_O^{\bullet\bullet}$.[42,55]
- Intervalence charge transfer (IVCT), involving electron exchange between dopant and matrix ions or between codopant ions, and multivalence charge transfer (MVCT), involving electron exchange between multiple-dopant ions and matrix ions, both without defect formation otherwise, represent underappreciated means of explaining valence changes.[56–69]
- Three types of colour centres (F^0, F^+, F^{++}) have been suggested by modelling[70] and validated experimentally for pure CeO_{2-x}.[71] While, the latter were generated at room temperature, high-energy irradiation often is required to create the Schottky pairs that are involved in the generation of such F-centres.[72] Doped CeO_{2-x} exhibits similar behaviour although this generally is attributed to an F-centre exchange (FCE) coupling mechanism involving magnetic dopant ions and $V_O^{\bullet\bullet}$.[73–75] These mechanisms also often are ignored sources of defects.

It is only in recent years that the instrumentation for the direct detection and quantitative analysis of these point defects has become widely available. Table 5 summarises these types of instrumentation and the data that can be generated with their use. The table is linked to a series of resultant images published largely by the authors of the present work (ESI,† Fig. S6–S11).

CeO_2 crystal growth mechanisms

The conventional perception of the crystal growth process under conditions of the generally used methods of precipitation and hydrothermal synthesis is that nanoparticles grow in two stages:[126] During processing, nucleation occurs in the precursor solution followed by subsequent growth of the resultant nuclei. Both of these stages can be controlled by varying the synthesis conditions to obtain nanoparticles of different morphologies, sizes, and degrees of crystallinity. The most commonly used experimental variables that determine these characteristics include the cerium concentration [Ce], usually from $Ce(NO_3)_3{\cdot}6H_2O$ as solute; sodium hydroxide concentration [NaOH] as precipitating agent; reaction temperature (T), invariably $\leq$200 °C; and reaction time (t), commonly $\leq$24 h. Since the first reports of the hydrothermal growth of CeO_2,[77–79] most studies have used the preceding conditions for synthesis, although alternative Ce salts as solutes,[15,78,80–93] and different precipitating agents[78,84–101] to generate these and alternative morphologies, including nanotubes,[80,82,94] nanoplates,[95] nanosheets,[96] nanorod flowers,[97] nanoneedles,[98] and solid and hollow nanospheres,[85,99–101] have been used.

Table 6 comprehensively surveys hydrothermal synthesis data for nanoceria morphologies, with variables [Ce] (*viz.*, [$Ce(NO_3)_3{\cdot}6H_2O$]), [NaOH], T, and t. Since sixteen of the previous eighteen studies used low [Ce] ($\leq$0.60 M) and limited [NaOH] ($\leq$22.5 M), the present work supplements these studies by using high [Ce] (2.00 M) and an extended range of high [NaOH] (7.0–35.0 M) concentrations. All of these studies involved the sole use of $Ce(NO_3)_3{\cdot}6H_2O$ and NaOH; no other salts were present.

Autoclave pressure

Although four variables have been specified, the use of hydrothermal syntheses introduces a fifth, which is vapour pressure (P). While, in the autoclave, this degree of freedom is fixed by the T and [NaOH] and so P is not considered, it remains an unknown. Fig. 7 completes the experimental picture by showing the internal autoclave vapour pressure at the ranges of T and [NaOH] regularly used. These data were interpolated from the Othmer diagram for NaOH aqueous solutions.[102]

Other considerations

A final issue is the potential for the effects of the use of other salts as the sources of Ce, such as $CeCl_3{\cdot}7H_2O$, and other precipitating agents, such as NH_4OH. Such species may play important roles in altering or directing the development of

Table 4 Potential CeO_{2-x} defect equilibria (using Ta as donor and Mn as acceptor dopant examples)

Defect equilibria	Solid solubility	Dopant	Charge compensation: Ionic	Charge compensation: Electronic
Intrinsic			Chemical	
	Oxygen vacancy formation		$2Ce_{Ce}^{\times} + 4O_O^{\times} \xrightarrow{CeO_2} 2Ce'_{Ce} + 3O_O^{\times} + V_O^{\bullet\bullet} + 1/2O_2(g)$	$Ce_{Ce}^{\times} + 2O_O^{\times} \xrightarrow{CeO_2} Ce'_{Ce} + 2O_O^{\times} + h^{\bullet}$
	Cerium vacancy formation		$[4Ce'_{Ce}] + \{6O_O^{\times} + 2V_O^{\bullet\bullet} + O_2(g)\} \xrightarrow{CeO_2}$ $\{4Ce_{Ce}^{\times} + V_{Ce}^{''''} + Ce_S^{\times}\} + \{6O_O^{\times} + 2V_O^{\bullet\bullet} + O_2(g)\}$	$[4Ce'_{Ce}] + \{6O_O^{\times} + 2V_O^{\bullet\bullet} + O_2(g)\} \xrightarrow{CeO_2}$ $\{4Ce_{Ce}^{\times} + V_{Ce}^{''''} + Ce_S^{\times}\} + \{8O_O^{\times} + 4h^{\bullet}\}$
	Schottky pair formation		$Ce_{Ce}^{\times} + 2O_O^{\times} \xrightarrow{CeO_2}$ $V_{Ce}^{''''} + Ce_S^{\times} + 2V_O^{\bullet\bullet} + O_2(g)$	$Ce_{Ce}^{\times} + 2O_O^{\times} \xrightarrow{CeO_2}$ $V_{Ce}^{''''} + Ce_S^{\times} + O_O^{\times} + V_O^{\bullet\bullet} + 1/2O_2(g) + 2h^{\bullet}$
	Frenkel defect formation		Ce interstitial: $Ce_{Ce}^{\times} + 2O_O^{\times} \xrightarrow{CeO_2} Ce_i^{\bullet\bullet\bullet\bullet} + V_{Ce}^{''''} + 2O_O^{\times}$ O interstitial: $Ce_{Ce}^{\times} + 2O_O^{\times} \xrightarrow{CeO_2} Ce_{Ce}^{\times} + 2O_i'' + 2V_O^{\bullet\bullet}$	
	Intrinsic ionisation		$[2Ce_{Ce}^{\times} + 2Ce'_{Ce}] + 7O_O^{\times} + V_O^{\bullet\bullet} + 1/2O_2(g) \xrightarrow{CeO_2} [2Ce'_{Ce} + 2Ce_{Ce}^{\times}] + 7O_O^{\times} + V_O^{\bullet\bullet} + 1/2O_2(g)$	
			Electrochemical	
	Acidic conditions		$2Ce_{Ce}^{\times} + 4O_O^{\times} + 2H^{\bullet}(aq) + 2e'(ext) \xrightarrow{CeO_2} 2Ce'_{Ce} + 3O_O^{\times} + V_O^{\bullet\bullet} + H_2O(aq)$	
	Basic conditions		$4Ce_{Ce}^{\times} + 8O_O^{\times} + H_2O(aq) + 2e'(ext) \xrightarrow{CeO_2} 4Ce'_{Ce} + 6O_O^{\times} + 2V_O^{\bullet\bullet} + 2OH'(aq) + 1/2O_2(g)$	
Extrinsic	Subst.	Donor	$2Ta_2O_5 \xrightarrow{CeO_2} 4Ta_{Ce}^{\bullet} + V_{Ce}^{''''} + 5Ce_S^{\times} + 10O_O^{\times}$	$Ta_2O_5 \xrightarrow{CeO_2} 2Ta_{Ce}^{\bullet} + 2Ce_S^{\times} + 4O_O^{\times} + 1/2O_2(g) + 2e'$
		Acceptor	$Mn_2O_3 \xrightarrow{CeO_2} 2Mn'_{Ce} + V_O^{\bullet\bullet} + 2Ce_S^{\times} + 2O_O^{\times} + 1/2O_2(g)$	$Mn_2O_3 + 1/2O_2(g) \xrightarrow{CeO_2} 2Mn'_{Ce} + 2Ce_S^{\times} + 4O_O^{\times} + 2h^{\bullet}$
	Inter.	Donor	$2Ta_2O_5 \xrightarrow{CeO_2} 4Ta_i^{\bullet\bullet\bullet\bullet\bullet} + 5V_{Ce}^{''''} + 5Ce_S^{\times} + 10O_O^{\times}$	$Ta_2O_5 \xrightarrow{CeO_2} 2Ta_i^{\bullet\bullet\bullet\bullet\bullet} + 4O_O^{\times} + 1/2O_2(g) + 10e'$
		Acceptor	$2Mn_2O_3 \xrightarrow{CeO_2} 4Mn_i^{\bullet\bullet\bullet} + 3V_{Ce}^{''''} + 3Ce_S^{\times} + 6O_O^{\times}$	$Mn_2O_3 + 1/2O_2(g) \xrightarrow{CeO_2} 2Mn_i^{\bullet\bullet\bullet} + 4O_O^{\times} + 6e'$
	Oxygen Interstitial Formation		$[2Ce'_{Ce}] + [3O_O^{\times} + V_O^{\bullet\bullet} + 1/2O_2(g)] + 1/2O_2(g) \xrightarrow{CeO_2} [2Ce_{Ce}^{\times}] + [4O_o^{\times}] + [O_i'' + 2h^{\bullet}]$	
IVCT & MVCT	Subst.	Donor	$Ce'_{Ce} + Ta_{Ce}^{\bullet} \xrightarrow{CeO_2} Ce_{Ce}^{\times} + Ta_{Ce}^{\times}$ or $Ce^{3+} + Ta^{5+} \rightarrow Ce^{4+} + Ta^{4+}$	
		Acceptor	$Ce_{Ce}^{\times} + Mn'_{Ce} \xrightarrow{CeO_2} Ce'_{Ce} + Mn_{Ce}^{\times}$ or $Ce^{4+} + Mn^{3+} \rightarrow Ce^{3+} + Mn^{4+}$	
	Inter.	Donor	$Ce'_{Ce} + Ta_i^{\bullet\bullet\bullet\bullet\bullet} + V_{Ce}^{''''} + Ce_S^{\times} \xrightarrow{CeO_2} Ce_{Ce}^{\times} + Ta_i^{\bullet\bullet\bullet\bullet} + V_{Ce}^{''''} + Ce_S^{\times}$ or $Ce^{3+} + Ta^{5+} \rightarrow Ce^{4+} + Ta^{4+}$	
		Acceptor	$4Ce_{Ce}^{\times} + 4Mn_i^{\bullet\bullet\bullet} + 3V_{Ce}^{''''} + 3Ce_S^{\times} \xrightarrow{CeO_2} 4Ce'_{Ce} + 4Mn_i^{\bullet\bullet\bullet\bullet} + 3V_{Ce}^{''''} + 3Ce_S^{\times}$ or $Ce^{4+} + Mn^{3+} \rightarrow Ce^{3+} + Mn^{4+}$	
Colour centre	F^0-Centre		$Ce_{Ce}^{\times} + 2O_O^{\times} \xrightarrow{CeO_2} V_{Ce}^{''''} + Ce_S^{\times} + 2V_O^{\bullet\bullet} + O_2(g)$	
	F^+-Centre		$2Ce_{Ce}^{\times} + 4O_O^{\times} \xrightarrow{CeO_2} 2V_{Ce}^{''''} + 2Ce_S^{\times} + 4V_O^{\bullet\bullet} + 2O_2(g) \xrightarrow{CeO_2} V_{Ce}^{''''} + V_{Ce}''' + 2Ce_S^{\times} + V_O^{\bullet} + 3V_O^{\bullet\bullet} + 2O_2(g)$	
	F^{++} Centre		$Ce_{Ce}^{\times} + 2O_O^{\times} \xrightarrow{CeO_2} V_{Ce}^{''''} + Ce_S^{\times} + 2V_O^{\bullet\bullet} + O_2(g) \xrightarrow{CeO_2} V_{Ce}''' + Ce_S^{\times} + V_O^{\bullet} + V_O^{\bullet\bullet} + O_2(g)$	
			$2Ce_{Ce}^{\times} + 4O_O^{\times} \xrightarrow{CeO_2} 2V_{Ce}^{''''} + 2Ce_S^{\times} + 4V_O^{\bullet\bullet} + 2O_2(g) \xrightarrow{CeO_2} 2V_{Ce}''' + 2Ce_S^{\times} + V_O^{\times} + 3V_O^{\bullet\bullet} + 2O_2(g)$	

where: IVCT = intervalence charge transfer, MVCT = multivalence charge transfer, Subst. = substitutional, Inter. = interstitial, subscript = ion sublattice (element = sublattice site) or surface (S = surface), superscript = net charge (× = neutral, • = positive, ′ = negative), V = vacancy, e′ = electron, $h^{\bullet}$ = hole, (g) = gas, (aq) = aqueous, (ext) = externally imposed, $V_O^{\bullet\bullet}$ = F^0-centre, $V_O^{\bullet}$ = F^+-centre, $V_O^{\times}$ = F^{++}-centre.

different morphologies. However, as stated, Table 6 reports data only for the use of $Ce(NO_3)_3{\cdot}6H_2O$ and NaOH as raw materials.

The range of CeO_2 morphologies often is uncertain owing to difficulties in imaging ultrafine grains, agglomeration, irregular shape outlines, and nonisometric facet outlines.[103] These challenges have resulted in reports of morphologies described as nanopolyhedra[104] and nanoparticles,[16] where these appear to be ultrafine simple octahedra or truncated octahedra. Further, there may be up to three variants of nanorods, one square[105] and possibly two hexagonal.[106] Unusually, these nanorods do not exhibit true prismatic cross sections as the optical mineralogy forms include pinacoids and rhombic prisms, often of similar dimensions, although the nanorods appear to exhibit identical growth directions.[105–107] In some cases, these nanorods have been reported to consist of $Ce(OH)_3$ while wet, oxidising to CeO_2 upon drying.[15,16,80,104,108]

The studies by Du *et al.*[106] and Nabavi *et al.*[109] are important because these are the only works to demonstrate the formation of metastable nanochains of individual crystallites of truncated nano-octahedra during heating at 100 °C[106] or at room temperature.[109] These are precursors that self-assemble and coalesce into square and hexagonal nanorods. However, two growth directions for hexagonal

Table 5 Analytical techniques applicable for the characterisation of structural defects, particularly in CeO_{2-x}

Technique	Acronym	Depth of penetration	Beam diameter/ field of view	Information provided	Fig.
X-ray diffraction	XRD	~10–60 μm	≤1 cm	• Lattice parameter changes from, *e.g.*, doping • Lattice parameter changes from $Ce^{4+} \leftrightarrow Ce^{3+}$ redox, where the charge compensation for $V_O^{\bullet\bullet}$ formation results in lattice expansion from the formation of Ce^{3+} • Structural destabilisation, as shown by peak broadening	S6
Laser Raman microspectroscopy	—	~1–3 μm	~1 μm	• Relative concentration of $V_O^{\bullet\bullet}$ due to quantum confinement, as shown by peaks at ~580 (D) cm^{-1} and ~1147 (2LO) cm^{-1} • Relative concentration of $V_O^{\bullet\bullet}$ also shown by blue shift and asymmetrical broadening of F_2g vibrational mode at ~464 cm^{-1}	S7 and S8
Photoluminescence	PL	~1–3 μm	~1 μm	• Surface electron/hole recombination rate, where $V_O^{\bullet\bullet}$ from either shallow or deep trapping sites (midgap states) that facilitate or inhibit electron/hole recombination, respectively	S9
Electron paramagnetic/ spin resonance spectroscopy	EPR/ESR	8 cm	~50 × 50 μm^2	• Semiquantitative analysis of unpaired electrons (radicals) associated with different defects	S9
X-ray photoelectron spectroscopy	XPS	1–3 nm	500 μm	• Quantitative analysis by deconvolution of 3*d* orbitals of Ce^{4+} and Ce^{3+} • Quantitative analysis by deconvolution of O1s orbital of oxygen bonded to Ce^{4+} and Ce^{3+} • Calculation of $V_O^{\bullet\bullet}$ concentration through 2 : 1 ratio of Ce^{3+} : $V_O^{\bullet\bullet}$ • Relative valence changes, as shown by peak shifts • Gap between valence band (VB) and Fermi level (E_f) • Identification of trapping states (deriving from defects) near VB	S9
Transmission Electron Microscopy	TEM	~100 nm	~100 nm ~1 × 1 μm^2	• Imaging of line, planar, and volume defects • Determination of lattice spacings to confirm identify of phases and to identify surface crystallographic planes • Quantification of lattice distortion • Identification of superlattice formation	S9
Energy Dispersive Spectroscopy	EDS (TEM)	—	1 × 1 nm^2 to ~1 × 1 μm^2	• Mapping of impurities • Assessment of compositional variation across interfaces	
Selected area electron diffraction	SAED	~100 nm	~100 nm ~1 × 1 μm^2	• Differentiation of transition between amorphous and crystalline conditions • Differentiation between polymorphic phases • Determination of lattice parameters for phase identification and lattice expansion/contraction, particularly for $Ce^{4+} \leftrightarrow Ce^{3+}$ redox	S9
Scanning tunnelling electron microscopy	STEM	~100 nm	~100 nm ~1 × 1 μm^2	• Suitable for the detection of $V_O^{\bullet\bullet}$ owing to sensitivity to light elements • Mapping of $V_O^{\bullet\bullet}$ distribution at atomic resolution • Mapping of local strain field resulting from lattice expansion from formation of $V_O^{\bullet\bullet}$ and associated $Ce^{4+} \rightarrow Ce^{3+}$ reduction	S10
Electron energy loss spectroscopy	EELS	~5 nm	~3–100 nm	• Quantitative analysis of $V_O^{\bullet\bullet}$ from the ratio of the intensities of two principal peaks, where the ratio is bounded by the minimal value of ~0.9 for stoichiometric CeO_2 ($[V_O^{\bullet\bullet}] = 0\%$) and the maximal value of ~1.25 for $CeO_{1.5}$ (CeO_{2-x} with the theoretical maximal $[V_O^{\bullet\bullet}] = 25\%$)	S11
High-angle annular dark field spectroscopy	HAADF	—	~1 × 1 nm^2 to ~50 × 50 nm^2	• Suitable for the detection of Ce vacancies $\left(V_{Ce}^{''''}\right)$ owing to sensitivity to heavy elements • Imaging of $V_{Ce}^{''''}$ and clusters at atomic resolution	S11
Energy dispersive spectroscopy	EDS (HAADF)	—	1 × 1 nm^2 to ~50 × 50 nm^2	• Mapping of impurities • Assessment of compositional variations across interfaces • Mapping of cerium and $V_O^{\bullet\bullet}$ distributions within and between crystallites through relative concentrations of ions • Mapping of individual Ce^{4+} and Ce^{3+} ions at atomic resolution	
Amplitude-modulated Kelvin probe force microscopy	AM-KPFM	—	~20 × 20 μm^2	• Construction of complete energy band diagram through combination of AM-KPFM (work function Φ – vacuum level to Fermi level, E_f) in conjunction with XPS (VB to E_f) and UV-Vis spectra (band gap, E_g)	S11

nanorods have been suggested, these being the commonly observed [110][16,106,108,110,111] and the less commonly observed [211].[106,111]

Despite many studies using hydrothermal synthesis to generate different nanoceria morphologies, the summary of Table 6 shows that many uncertainties remain. Although several proposals concerning possible growth mechanisms have been conjectured,[15,16,106,112,113] these remain poorly understood owing to insufficient data for mechanistic validation.

Supplementary experimentation

Electron microscopy

Fig. 8(a) and (b) show two of the variants of the hexagonal nanorod cross sections, which confirm the nature of the hexagonal nanorods as nonprismatic (ESI,† Fig. S2). These are consistent with the two equilibrium shapes predicted by Wulff constructions considered previously.[122–124] TEM analyses

Table 6 Summary of effects of Ce concentration (using $Ce(NO_3)_3{\cdot}6H_2O$), NaOH concentration, temperature, and time on resultant morphologies of nanoceria from hydrothermal synthesis (and precipitation)

[Ce] (M)	[NaOH] (M)	Ageing time	Temp. (°C)	Morphology	Note	Ref.
0.0016	0.11	—	25	Truncated octahedra	A	Kamimura *et al.*[114]
0.0052	0.38			Truncated octahedra		
0.0259	1.88			Truncated octahedra		
0.01	0.15	24 h	25	Simple octahedra + truncated octahedra	B	Liu *et al.*[107]
0.03	0.03	24 h	180	Simple octahedra + truncated octahedral	—	Lin *et al.*[115]
	0.08			Truncated octahedra		
	0.10			Truncated octahedra		
	0.13			Truncated octahedra		
	0.33			Truncated octahedra		
0.10	0.10			Truncated octahedra		
0.05	0.01	24 h	100, 180	Truncated octahedra	C	Mai *et al.*[104]
	1.00, 3.00		100	Truncated octahedra + square rods		
	6.00, 9.00		100	Square rods	—	
	6.00		140	Square rods + cubes		
			180	Cubes		
0.10	1.00	10 h	100–150	Truncated octahedra + square rods	—	Torrente-Murciano *et al.*[17]
	2.00–10.0		150	Square rods		
	4.00–10.0		<100	Truncated octahedra		
	<5.00		180	Truncated octahedra + square rods + cubes		
	10.0–15.0		70	Square rods		
	15.0		180	Cubes		
0.13	0.45	24 h	90	Truncated octahedra	—	Lykaki *et al.*[118]
	2.75			Truncated octahedra + square rods		
	0.45		180	Cubes		
0.35	0.01	—	25	Simple Octahedra + truncated octahedra	B	Zhou *et al.*[105]
	2.00	10 h	100	Square rods	—	
0.40	6.90	7 h	100	Hexagonal rods	—	Guo and Zhou[117]
		15 h		Hexagonal rods		
		24 h		Hexagonal rods		
		48 h		Hexagonal rods		
0.40	6.90	24 h	100	Square rods	—	Li *et al.*[118]
0.40	6.90	24 h	100	Square rods	D	Wu *et al.*,[119] Liu *et al.*[120]
			180	Cubes		
0.40	7.20	24 h	180	Cubes	E	Wu *et al.*[15]
0.45	<10.0	24 h	<70	Truncated octahedra	—	Mehmood *et al.*[12]
	10.0		100–150	Square rods		
	5.00–20.0		180-200	Cubes		
0.45	10.0	24 h	180	Cubes	—	Bhatta *et al.*[121]
0.45–0.60	<5.00	24 h	<100	Simple octahedra	F	Sakthivel *et al.*[16,111]
	5.00–22.5		50–150	Hexagonal rods	G	
			150–200	Cubes	—	
0.50	15.0	24 h	100	Hexagonal rods	H	Agarwal *et al.*[110]
			180	Cubes		
2.00	0.80	12 min	100	Truncated octahedra chains	I	Du *et al.*[106]
	2.00			Truncated octahedra chains		
	>5.00			Hexagonal rods		
2.00	14.0	40 days	5	Hexagonal rods	—	Present work
		30 min	50–200	Hexagonal rods		
		1–2 h	50–100	Hexagonal rods		
		1 h	150–200	Hexagonal rods + cubes		
		2 h	150	Hexagonal rods + cubes		
		2 h	200	Cubes		
	7.00	2 h	200	Hexagonal rods + cubes		
	14.0			Cubes		
	7.00–35.0	24 h	25	Hexagonal rods	J	
			100–150	Hexagonal rods + cubes	—	
			150–200	Cubes		

Table 6 (*continued*)

[Ce] (M)	[NaOH] (M)	Ageing time	Temp. (°C)	Morphology	Note	Ref.
3.20	14.0	—	25	Particles	B, K	Pan *et al.*[108]
		72 h	100	Tubes	L	
		24 h	110	Wires	M	
			120	Truncated octahedra	—	
			140	Truncated octahedra + cubes		
			160	Cubes		
		2 h	180	Truncated octahedra + hexagonal rods + cubes	N	
		24 h		Cubes	—	

(A) By precipitation over 2 h without reported ageing. (B) By precipitation over 2 h followed by ageing for 24 h at 25 °C. (C) Nanopolyhedra described as nanooctahedra. (D) Wu *et al.*[119] $Ce(NO_3)_3{\cdot}6H_2O$ + NaOH gave nanorods and nanocubes but $Ce(NO_3)_3{\cdot}6H_2O$ + $Na_3PO_4{\cdot}12H_2O$ gave nanooctahedra; Liu *et al.*[120] $Ce(NO_3)_3{\cdot}6H_2O$ + NaOH gave nanorods and nanocubes but $Ce(NO_3)_3{\cdot}6H_2O$ + CH_3COONH_4 gave nanooctahedra. (E) $Ce(NO_3)_3{\cdot}6H_2O$ + NaOH gave nanocubes but $CeCl_3{\cdot}7H_2O$ gave nanorods. (F) Term nanoparticles used but TEM images show nanooctahedra. (G) Hexagonal → square nanorod conversion mechanism proposed. (H) Uncertainty about cross sectional shape of rods since (111) facets indicated hexagonal rods but HAADF imaging suggested rectangular cross section. (I) Two variants: Both chains and hexagonal rods oriented in growth direction [110] or [211]. (J) By precipitation over 10–30 min followed by 24 h ageing at 25 °C. (K) Suggested mechanism (Scheme 1 in ref. 108) indicates that the nanoparticles were the decomposition product of nanotubes or nanowires. (L) Morphology of nanotubes not specified. (M) Nanowires stated to form by deposition on nanotube ends. (N) Hexagonal nanorods assumed on basis of use of high [Ce].

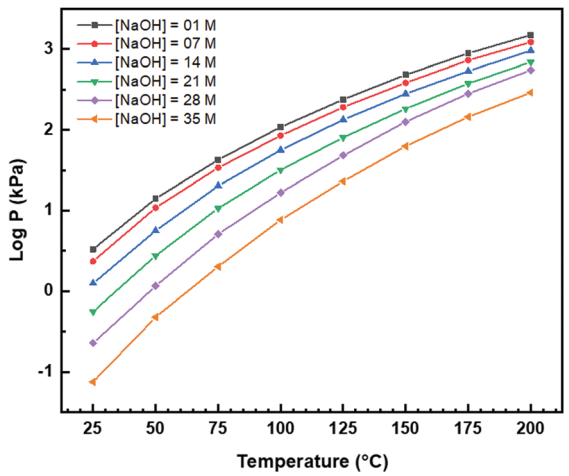

Fig. 7 Autoclave vapour pressure (*P*) at different [NaOH] and *T* determined from Othmer diagram for NaOH aqueous solutions.[102]

reveal that the prism cross sections are bounded by four {111} facets and two {100} facets; each of the *c* axis terminations consists of pyramids containing four {111} facets (other two unknown); the growth directions are ⟨110⟩, as observed previously.[16,106,108,110,111]

The presence of ~100 nm nanospheres was observed occasionally under the synthesis conditions of *T* = 75–125 °C and [NaOH] = 14.0–35.0 M. In agreement with others,[96,125] these were found to be single-crystal. Fig. 8(c) reveals the mechanism by which this singular morphology (spheroids) develops, which is by the self-assembly, intergrowth, and coalescence of self-assembled precursor crystallites. The resultant single-crystal nanospheres were established at sizes in the range ~20–50 nm diameter, with the larger size's being predominant. The same mechanism appears to apply to {111}-truncated nanocubes (cuboids) as shown in Fig. 8(d), which coalesce and form truncated nanocubes (ESI,† Fig. S3(a) and (b)). Further, simple cuboids also form by this mechanism (ESI,† Fig. S3(c) and (d)). The cuboids were of variable size (commonly ~20–30 nm but as large as 165 nm when coalesced) but they were less common than the nanospheres.

Assuming that the fast Fourier transformation (FFT) patterns (Fig. 8(c) and (d)) indicate exposed facets of the crystallites, then the spheroids are likely to be octahedron-like, comprised of multiple crystallites with mutual {111} interfaces, and the cuboids are likely to be cube-like, comprised of multiple crystallites with mutual {100} interfaces. The outlines of the latter morphology are indistinct but the detection of multiple examples of these confirms that they are consistent forms (ESI,† Fig. S3(c) and (d), ESI†).

The principal differences between these formation conditions are that the spheroids|nanospheres formed at lower temperatures (75–125 °C) and higher [NaOH] (14.0–35.0 M) than the cuboids|truncated nanocubes, which formed at higher temperature 100–125 °C and lower [NaOH] (14.0–21.0 M). However, established truncated nanocubes of sizes much smaller (~4–5 nm) than observed for the cuboids were observed commonly. Since such a size differential was not observed for the nanospheres, then there may be a size effect for the formation of cuboids according to *T* and *t* effects, although the data do not rule out this possibility for the spheroids as well. These morphological effects are interpreted in terms of thermal vibrations, where low intensities would facilitate self-assembly, intergrowth, and coalescence, thus allowing the formation of the larger spheroids and established nanospheres while the greater disturbance from high intensities would limit formation to the smaller forms of cuboids and established truncated nanocubes (but possibly nanospheres as well).

The species subject to thermal vibrations, which intergrow, self-assemble, and coalesce to establish the final established forms, are crystallites that are generated by the disassembly of the nanorods, as shown in Fig. 8(e) and (f). This process is shown more clearly in Fig. 8(g) and (h). These four images demonstrate that the hexagonal nanorods are destabilised and deteriorate under the conditions of both low temperature (5 °C)|long time (40 days) and high temperature (200 °C)|short time (1.5 h).

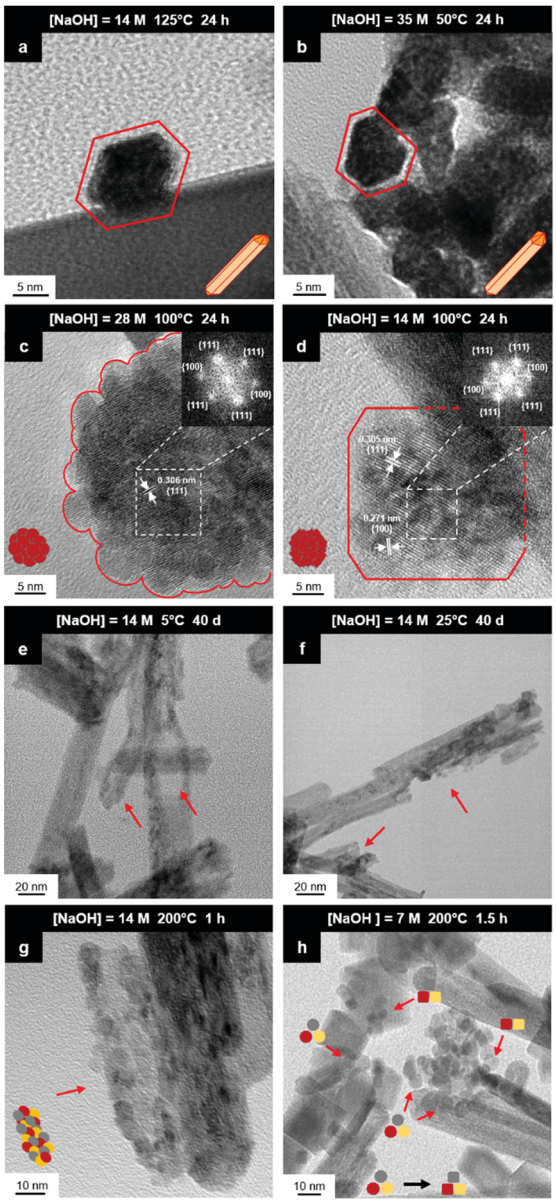

Fig. 8 HRTEM images: (a) nanorod with elongated hexagonal cross section; (b) nanorod with asymmetric hexagonal cross section; (c) crystallites self-assembled into intergrown spheroid nanoparticle; (d) crystallites self-assembled into intergrown truncated cuboid nanoparticle; TEM images: (e and f) hexagonal nanorods exhibiting nanostructural destabilisation (red arrows) at low temperature|long time and high temperature|short time; (g) hexagonal nanorods destabilised into rounded crystallites (red arrow); (h) faceting (red arrows) of rounded crystallites into octahedral spheroids (decagons) and cuboids (squares), followed by NO_3^- anion selective adsorption to convert the former to the latter (black arrow) (authors' unpublished work).

Crystal growth

In conventional crystal growth by precipitation, it is assumed that each individual nucleus acts as a potential source of epitaxial growth.[126] In contrast, the present work suggests an interposing four- or five-stage process of some difference:

(1) Disassembly by destabilisation and deterioration
(2) Resultant establishment of independent crystallites
(3) Possible adsorptive alteration of the crystallite morphology
(4) Crystallite self-assembly
(5) Crystallite coalescence into established grain

This process effectively introduces an unrecognised intermediate stage of crystal growth between those of nucleation and grain establishment. For Stage 3, high temperatures favour NO_3^- anion selective adsorption[15] and alteration of octahedral spheroidal crystallites (decagons) into cuboidal crystallites (squares) and nanocube establishment. When the temperature is insufficient to activate NO_3^- anion selective adsorption on {100}, retention of octahedral spheroidal crystallites and nanosphere establishment occur, precluding Stage 3. The observed morphologies of the nanosphere and nanocube variants are shown in Fig. 9; the truncations on the nanocubes are too small to image at these magnifications (ESI,† Fig. S3(a) and (b)).

$Ce(OH)_3$ nanorods

Zhou *et al.*[80] suggested a solution-reprecipitation process for the conversion of what were assumed to be $Ce(OH)_3$ nanorods in 15% H_2O_2 at room temperature to CeO_2 nanotubes. Wu *et al.*[15] and Mai *et al.*[104] used X-ray diffraction (XRD) to identify hexagonal $Ce(OH)_3$ nanorods hydrothermally synthesised from $CeCl_3{\cdot}7H_2O$ and NaOH and from $Ce(NO_3)_3{\cdot}6H_2O$ and NaOH, respectively. Both studies[15,104] reported a $Ce(OH)_3 \rightarrow CeO_2$ nanorod conversion upon oxidation. Wu *et al.*[15] reported the conversion of nanorods to nanocubes by NO_3^- adsorption on {100}. Ji *et al.*[127] noted the importance of the anions in solution to the CeO_2 morphology formed, although they considered the anions in terms of oxidation rather than selective adsorption.

Sakthivel *et al.*[16] reported the fabrication of what were assumed to be $Ce(OH)_3$ hexagonal nanorods, although these were considered to be metastable, converting to nanocubes at higher temperatures, both morphologies of which converted to CeO_2 upon drying. Pan *et al.*[107] reported the synthesis of what were assumed to be $Ce(OH)_3$ nanorods, which oxidised under hydrothermal conditions to CeO_2. They proposed a conversion mechanism for nanowires of mixed Ce^{4+}/Ce^{3+} valences into apparently stable equiaxed nanoparticles of ~15 nm size, with conversion of these into nanocubes at higher temperatures. This mechanism is problematic in that it contradicts the three published morphology maps,[12,16,17] which show that increasing temperatures result in a stepwise conversion as follows:

Nanooctahedra → Nanorods → Nanocubes

These three reports[12,16,17] did not provide supporting microscopy evidence for the suggested mechanisms.

Nanochains

A key point of these mechanisms is the nature of the crystallites, which are illustrated in Fig. 10 as rhomboids (simple octahedra), octahedra ({100} truncated octahedra), and decagons ({110} and {100} truncated octahedra). As will be explained subsequently, these crystallites consist of $Ce(OH)_4$ precipitates. The roles of the simple octahedral and truncated octahedral crystallites are critical to the formation of nanochains (at 100 °C (ESI,† Fig. S4[106]) or at room temperature),[109] which act as precursors to the square and hexagonal nanorods, respectively. The proposed

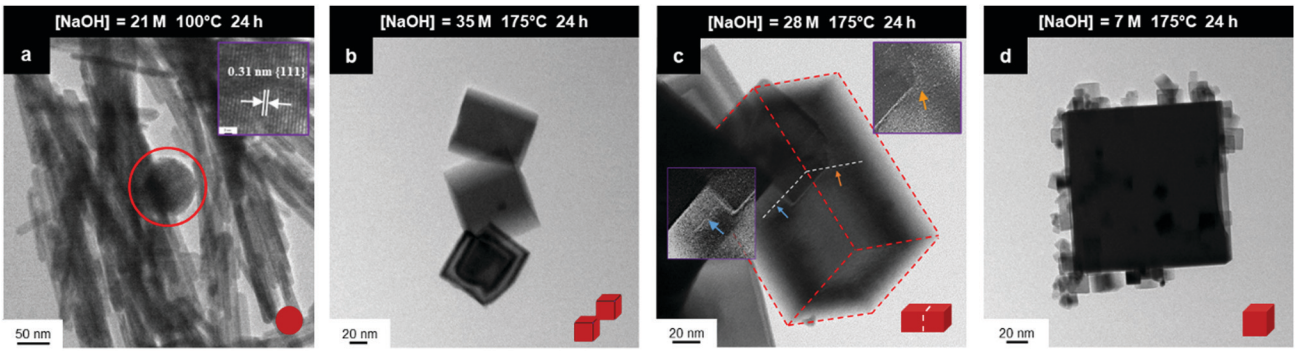

Fig. 9 TEM images: (a) sphere (circled) (b) intergrowths, (c) multicubes, (d) cubes with adsorbed smaller CeO_2 nanocubes (authors' unpublished work).

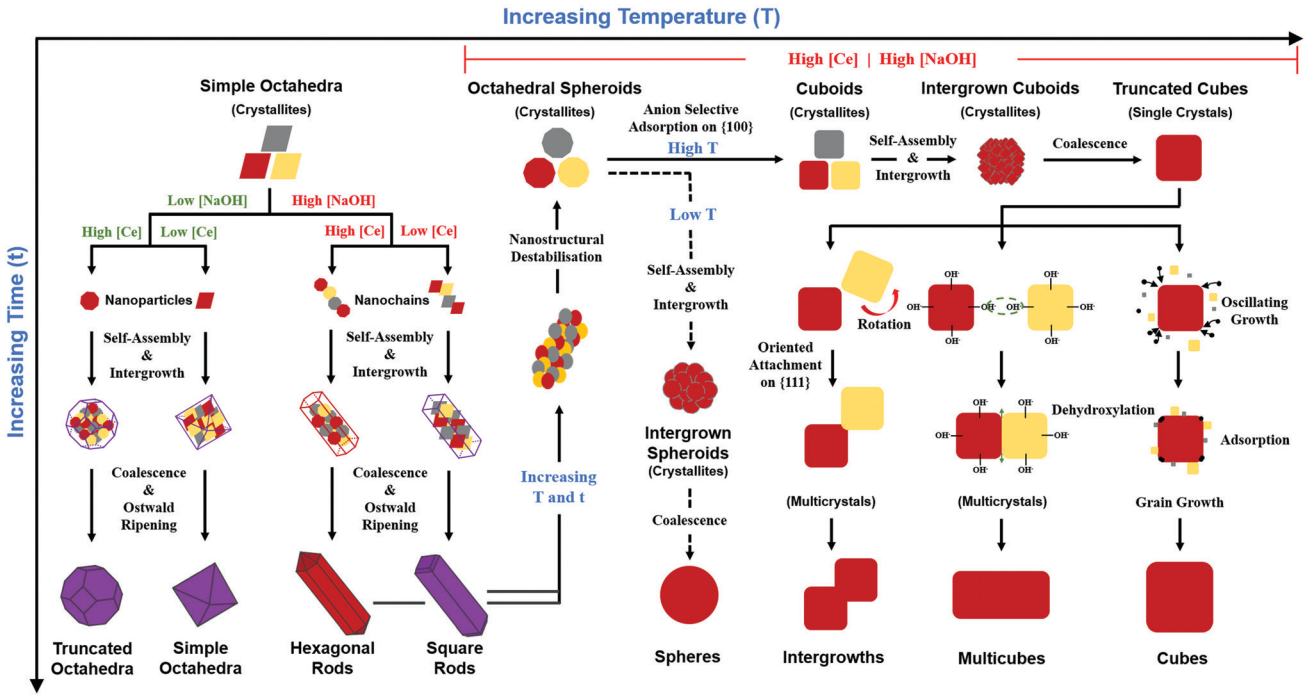

Fig. 10 Schematic of growth mechanisms of CeO_{2-x} nanomorphologies (red/yellow = investigated; purple = from the literature; [Ce]: low < 0.50 M ≤ high | [NaOH]: low < 5.00 M ≤ high | *T*: Low < 150 °C ≤ high | *t*: short ≤ 2 h < long.

nanochain-to-nanorod conversion mechanisms are illustrated in Fig. 11. A summary of the reports of the resultant crystallographies of the two types of nanorods is given in Table 7.

The conversion of the $Ce(OH)_4$ precipitates into nanochains and then square or hexagonal nanorods through the development of different crystallographic planes can be interpreted in consideration of the data given in Table 2, which show that the order of stability of the relevant planes is {100} < {110} < {111}, as also will be discussed subsequently.

Square nanorods

For the nanochains of simple octahedra of $Ce(OH)_4$, the uniquely present {111} planes undergo face-to-face adsorption through anionic ligand bonding, which subsequently condenses. As these are the only planes available, then their mutual adsorption is the only option. The driving force for this adsorption is surface energy reduction by partial annihilation of two planes, resulting in the formation of a zigzag nanostructure, which has been observed before for simple octahedra.[128–130] Decreasing surface area (and attendant surface energy) is a similar driving force for the octahedra to form {110} and {100} truncations on the outer surfaces. Subsequently, coalescence of the octahedra and Ostwald ripening result in the formation of a square nanorod with the commonly observed tetragonal prism consisting of single {110} and {100} pinacoids and the consistently observed ⟨110⟩ growth directions.[12,15–17,104,105,116,118–120,131]

Hexagonal nanorods

In the case of the nanochains of truncated octahedra of $Ce(OH)_4$, the less stable planes are {100},[33,34,36] which are polar, unlike nonpolar {111}.[132,133] The low stability and presence of the dipole for the former of these two oxygen-terminated (and hence negatively charged) planes[134–137] explain the preferential adsorption of the anionic ligand on the {100} planes;

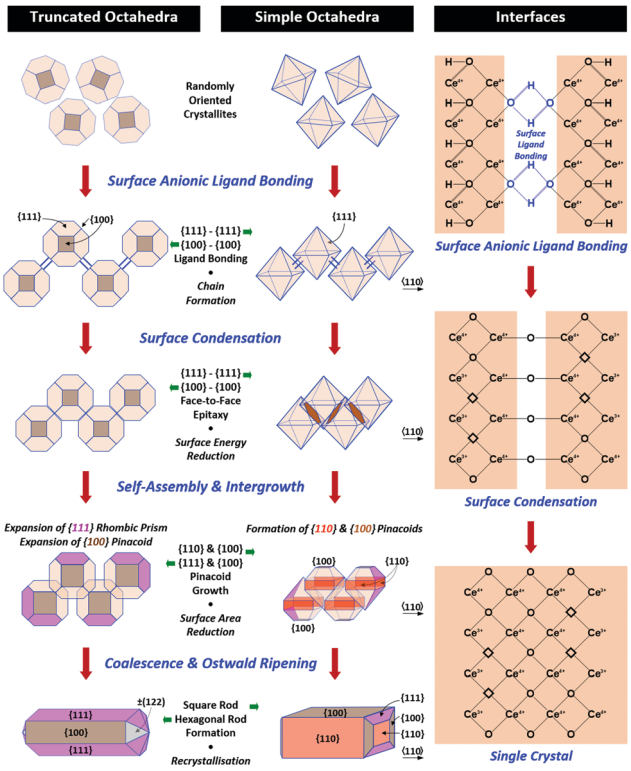

Fig. 11 Proposed mechanisms for conversion of nanochains into square and hexagonal nanorods (hydroxyl bonding is shown as a simplification of the probable anionic ligand bonding).

this epitaxial attachment has been observed before.[138] So face-to-face adsorption occurs by the preceding processes but with annihilation of {100} planes, again resulting in a zigzag nanostructure, which is required for ⟨110⟩ growth directions. The surface area decreases through growth of the outer {111} and remaining {100} planes, followed by coalescence and Ostwald ripening to establish a single crystal with a hexagonal prism consisting of a {111} rhombic prism and a {100} pinacoid, again with ⟨110⟩ growth directions. This mechanism is supported by the observation by Du *et al.*[106] (Table 6) of the alteration of nanochains of truncated octahedra to hexagonal nanorods with increased [NaOH].

The starting point for the assessment of the growth mechanisms for square nanorods and hexagonal nanorods is the ⟨110⟩ growth directions for both types. This is a key observation because both growth mechanisms must meet this criterion. For simple octahedra, only {111} planes are available and so only the zigzag nanostructure would result in ⟨110⟩ growth. In the case of the truncated nanorods, if the commonly observed {100} truncations were aligned linearly, this corner-to-corner growth would not result in ⟨110⟩ growth. However, while {110} octahedral truncations are less commonly observed, they quality as being suitable for ⟨110⟩ edge-to-edge growth. However, this is considered unlikely for the two reasons that (1) Table 2 shows that {110} planes are more stable than {100} planes, so annihilation of the latter is more probable and (2) {110} truncations are not observed commonly but hexagonal nanorods are.

Table 7 Crystallographies of CeO_2 nanorods using $Ce(NO_3)_3{\cdot}6H_2O$ and NaOH by precipitation and hydrothermal synthesis

Square CeO_2 nanorods				
Growth directions	Tetragonal prism			
	Pinacoid A	Pinacoid B	Note	Ref.
[001]	(100)	(010)	A	—
⟨110⟩	{110}	{100}	—	Mehmood *et al.*[12]
				Wu *et al.*[15]
				Sakthivel *et al.*[16]
				Torrente-Murciano *et al.*[17]
				Mai *et al.*[104]
				Zhou *et al.*[105]
				Lykaki *et al.*[116]
				Li *et al.*[118]
	{111}	{100}	B	Wu *et al.*[119]
				Wang *et al.*[131]
	—	—	—	Liu *et al.*[120]

Hexagonal CeO_2 nanorods				
Growth directions	Hexagonal prism			
	Rhombic prism	Pinacoid	Note	Ref.
[001]	{110}	{100}	C	—
⟨110⟩	{111}	{100}	—	Sakthivel *et al.*[16]
				Du *et al.*[106]
				Sakthivel *et al.*[111]
				Guo and Zhou[117]
				Present Work
	{111}	{111}	B	Agarwal *et al.*[110]
	—	—	—	Pan *et al.*[108]
⟨211⟩	{111}	—	D	Du *et al.*[106]
				Sakthivel *et al.*[111]

(A) True tetragonal prism, where both pinacoids are crystallographically equivalent to form a true prism in cubic symmetry (a_1, a_2, a_3). (B) Specified planes not crystallographically possible pairs. (C) True hexagonal prism, where rhombic prism and pinacoid are crystallographically equivalent to form a true prism in hexagonal symmetry (a_1, a_2, a_3, c). (D) Growth directions not crystallographically consistent with hexagonal prism planes (although ⟨211⟩ can be normal to {111}).

Oxygen vacancies

It is well known that $V_O^{\bullet\bullet}$ play a key role in the properties of CeO_{2-x}.[6,14,142–144] Table 4 confirms that there are many possible mechanisms by which $V_O^{\bullet\bullet}$ can form, although the previous text explains that undoped CeO_{2-x} exhibits intrinsic $V_O^{\bullet\bullet}$ that are charge compensated by $Ce^{4+} \rightarrow Ce^{3+}$ reduction. However, $V_O^{\bullet\bullet}$ also appear to play a role in CeO_{2-x} surfaces. This is indicated in the inset red cubes in Fig. 9(b), which show {111} planes with corner-to-corner joining. This is counter-intuitive as Table 2 shows that these planes are the most stable and therefore unlikely to annihilate in the presence of the less-stable {100} planes. The reason for the observation of this preferred joining is the additional surface energy provided by the roughness of the {111} truncations. This roughness develops owing to the lower stabilities of the {110} and {100} planes, which convert to subfacets of the more stable {111} planes under the destabilising influence of $V_O^{\bullet\bullet}$.[121,145]

Principal variables

The schematic of Fig. 10 formalises the effects of the four main processing variables [Ce] (thus fixing [NO_3^-]), [NaOH],

Table 8 Morphological data for CeO_2 fabricated by ligands alternative to NO_3^- by various methods

Anionic ligand	Morphology observed	Crystallographic data	Note	Ref.
Hydrothermal synthesis using NaOH precipitating agent				
Cl^-	Nanorods	[110] growth {110} & {100} faces	—	Wu *et al.*[15]
	Nanowires	(111) faces	—	Fu *et al.*[81]
	Nanotubes	[100] growth	—	Tang *et al.*[82]
	Nanoparticles	—	—	Kannan and Sundrarajanya[139]
$Cl^- + NO_3^-$	Nanocubes	—	—	Wu *et al.*[15]
Br^-	Nanorods	—	—	Wu *et al.*[15]
BrO_3^-	Nanoparticles	—	—	Wu *et al.*[15]
I^-	Nanorods	—	—	Wu *et al.*[15]
SO_4^{2-}	Nanooctahedra	—	—	Wu *et al.*[24]
	Nanorods	—	—	Wu *et al.*[15]
	Nanotubes	Polycrystalline	—	Zhou *et al.*[80]
Hydrothermal synthesis using NH_4OH precipitating agent				
Cl^-	Nanowires	{111} faces	—	Wang *et al.*[84]
	Nanorods	[110] growth	—	Vantomme *et al.*[86]
$Cl^- + NO_3^-$	Various	—	A	Wang *et al.*[84]
SO_4^{2-}	Nanoparticles	—	—	Hirano and Kato[78]
CH_3COO^-	Nanowires	Polycrystalline	—	Sun *et al.*[87]
Other synthesis methods and precipitating agents				
NO_3^-	Nanobelts	Polycrystalline	B	Rao *et al.*[140]
Cl^-	Nanooctahedra	—	C	Laberty-Robert *et al.*[88]
	Nanorods	[211] growth {111} & {100} faces	D	Ji *et al.*[89]
	Nanowires	Polycrystalline	E	Yan *et al.*[91]
	Nanospheres	Crystalline	F	Zarinkamar *et al.*[141]
$Cl^- + NH_2^-$	Hollow Nanospheres	Polycrystalline	E + G	Yang *et al.*[85]
	Nanorods	—	H	Sun *et al.*[90]
SO_4^{2-}	Rounded Nanoparticles	Polycrystalline	E	Hirano and Inagaki[92]
CH_3COO^-	Nanooctahedra	—	I	Liu *et al.*[120]
	Nanorods	⟨100⟩ growth	J	Lin *et al.*[93]

(A) Cl^-/NO_3^- ratio: 3/1 = nanowires + nanoparticles; 1/1 = rounded or cubic nanoparticles + nanowires; 1/3 = nanoparticles. (B) Precipitating agents NaOH + formaldehyde (CH_2O). (C) Gelation synthesis. (D–J) Hydrothermal syntheses with precipitating agents: (D) $Na_3PO_4{\cdot}6H_2O$, (E) urea ($CO(NH_2)_2$), (F) ethanol, (G) H_2O_2, (H) ethylenediamine ($C_2H_4(NH_2)_2$), (I) ammonium acetate (CH_3COONH_4), (J) oleyamine ($C_{18}H_{35}NH_2$).

temperature (thus fixing P), and time (ESI,† Fig. S5); Fig. 10 shows the different physicochemical mechanisms; and it combines the variables and mechanisms to explain the generation of the observed different morphologies and their variants. However, this schematic applies only to the commonly used raw materials $Ce(NO_3)_3{\cdot}6H_2O$ and NaOH; other morphological outcomes have been reported for the use of alternative, less commonly used, Ce salts as solutes (Table 8) and precipitating agents (Table 9).

Table 9 Morphological data for CeO_2 fabricated using $Ce(NO_3)_3{\cdot}6H_2O$ with precipitating agents alternative to NaOH by precipitation and hydrothermal synthesis

Precipitating agent	Morphology observed	Crystallographic data	Note	Ref.
H_2O_2	Nanoneedles	[100] growth	—	Tang *et al.*[98]
H_2O_2 + urea	Hollow nanospheres	Polycrystalline	A	Zhang *et al.*[100]
Urea	Nanorods	[110] growth {111} & {100} faces		Tang *et al.*[146]
	Nanocubes	{111} truncations		
NH_4OH	Nanooctahedra	—	—	Han *et al.*[93]
	Nanowires	{111} faces		
	Nanotubes	{111} faces		
	Nanooctahedra	—	—	Wang *et al.*[101]
$Na_3PO_4{\cdot}6H_2O$	Nanooctahedra	[100] growth	B	Yan *et al.*[147]
	Nanorods	{100} faces		
	Nanocubes			
	Nanooctahedra	—	—	Yu *et al.*[97]
	Nanorods	[100] growth		
$Na_3PO_4{\cdot}12H_2O$	Nanooctahedra	—	—	Liu *et al.*,[148] Wang *et al.*[131]
Organic acids	Solid nanospheres	Polycrystalline	—	Wang and Kobiro[99]

(A) Decomposition of urea considered to be a source of NH_3 gas bubbles to facilitate hollow nanosphere formation. (B) $Na_3PO_4{\cdot}6H_2O$ considered to be a mineraliser; crystallographic data for nanorods; nanocubes not illustrated but stated to form at pH > 10.

Crystallography and optical mineralogy

The data for the square nanorods are completely consistent (Table 7), revealing ⟨110⟩ growth directions and a tetragonal prism consisting of {110} and {100} pinacoids, thereby resulting in what actually is a rectangular cross section. Apparently, the only investigation reporting the tetragonal bipyramid is that by Mehmood *et al.*,[12] who identified {111} planes. Fig. 11 shows that the proposed growth mechanism indicates that this is as expected, as are the complementary {100} planes, each of which forms a dome.

The data for the hexagonal nanorods generally are consistent (Table 7). Although the most commonly observed crystallographic relation reveals ⟨110⟩ growth directions,[16,106,108,110,111] there are two reports of ⟨211⟩ growth directions.[106,111] However, both studies report ⟨211⟩ growth directions as being parallel to {111} planes, which is not crystallographically possible. Apart from these two reports, the hexagonal prism actually consists of a {111} rhombic prism and one {100} pinacoid.[16,106,108,111] There also is a single report of a hexagonal prism consisting of {111} planes[110] but this is not crystallographically possible. The nature of the hexagonal prism can be considered in terms of the internal angles between the planes:

$$\{111\} - \{100\}\ \text{Angle} = 125.26^\circ$$

$$\{111\} - \{111\}\ \text{Angle} = 109.47^\circ$$

It is clear that these planes cannot form a true hexagonal prism as this requires a single internal angle of 120°. These angular relations are supported by the sums of the six angles:

$$\text{True Hexagonal Prism: } 6(120.00^\circ) = 720.00^\circ$$

$$\text{Actual Hexagonal Prism: } 4(125.26^\circ) + 2(109.47^\circ) = 719.98^\circ$$

There are few comments concerning the hexagonal dipyramid terminating the hexagonal prism. The present work indicates that this consists of a {111} rhombic prism and one of the eight possible ±(122) pinacoids. The {111} planes have been confirmed by others,[109,110] who observed {111} facets on the ends of nanorods. As there do not appear to be any reports of a terminating {110} pedion or pinacoid normal to the family of principal ⟨110⟩ axes, then the hexagonal dipyramid must converge to a point, which requires all six of the planes to exhibit the same angle with the hexagonal prism planes. As the {111} − {111} angle is 109.47° and the only other possible plane with this angle is {100} − {122}, then the latter identifies the unknown pinacoid, as shown in grey in Fig. 11. However, this pinacoid cannot include the full family of {122} planes as the alternative ±(211) and ±(212) variants exhibit different angles, which confirms the unique pinacoid orientation (of the three possibilities). The formation of this pinacoid is supported by the high stability of the {122} plane shown in Table 2, which generally is second only to that of the {111} planes.

Anionic ligand

Other investigators have observed more limited morphological outcomes when the nanoparticles were synthesised using different Ce salts. A survey of these reports is given in Table 8. The importance of the anionic ligand, particularly NO_3^-, to the morphological development was recognised as long ago as 1996 by Hirano and Kato[78] and more recently has been reviewed by Zhang *et al.*[149] The hydroxyl bonding shown in Fig. 11 is a probable simplification of the actual ligand bonding in that the orientation relations that are established between the octahedral crystallites of the nanochains may be controlled by monodentate, bidentate, or mixed-ligand bonding with NO_3^-. In effect, the nature of the anionic ligands may be one of the factors determining the orientations of the nanochains, which in turn determine the crystallographic relations of the nanorods. It also is likely that (with the exceptions of the use of $Na_3PO_4{\cdot}6H_2O$[100] and urea $(CO(NH_2)_2)$[128] as precipitating agents), the formation of nanocubes is dependent on the selective adsorption of NO_3^- on the crystallites that form from the destabilisation and deterioration of the nanorods, as shown in Fig. 10.

Precipitating agent

The role the precipitating agent has not been examined probably because NaOH is used so commonly, as shown in Tables 6 and 8. Although Table 8 canvasses the use of other precipitating agents, salts other than $Ce(NO_3)_3{\cdot}6H_2O$ also have been used. Table 9 summarises reports on the use of this salt but with different precipitating agents. During the precipitation of a hydroxide (*viz.*, $Ce(OH)_4$), the cation of the precipitating agent (*viz.*, Na^+ *vs.* NH_4^+) would not be expected to play a direct chemical role in morphological development. However, alternative anions, such as NH_2^- (from urea,[85,91,92] ethylenediamine,[90] or oleyamine,[93] Table 8) and PO_4^{3-} (from $Na_3PO_4{\cdot}6H_2O$,[95,100] Table 9), would be expected to have an influence.

Summary of variables

In summary, there are seven general variables that determine the morphological development of CeO_2 during precipitation and hydrothermal synthesis (where the types of anion and precipitating agent are fixed in the present work and where T and [NaOH] fix the autoclave pressure (P)[102]):

- Concentration of parent Ce in soluble salt
- Type of anionic ligand of Ce salt
- Concentration of anionic ligand
- Type of precipitating agent
- Concentration of precipitating agent
- Temperature
- Time

Pourbaix diagram

According to the modified $Ce^{4+/3+}$–H_2O Pourbaix diagram, which was prepared for the $Ce^{4+/3+}$–Na^+–NO_3^-–H_2O system, shown in Fig. 12, the blue predominance region is for the crystallites that comprise the nanochains, which begin as precipitates of $Ce(OH)_4$ amorphous species (pt) and then convert readily to hydroxylated (s) and hydrated crystalline species (s) during aging, ultimately drying rapidly under oxidising conditions in the sequence:

$$Ce(OH)_4(pt) \rightarrow Ce(OH)_4(s) \rightarrow CeO_2{\cdot}2H_2O(s) \rightarrow CeO_2(s)$$

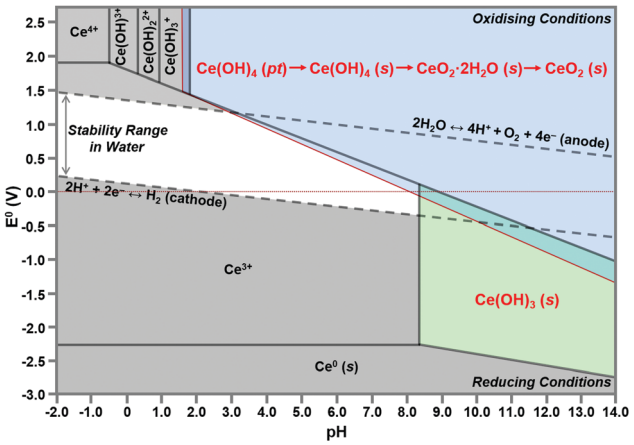

Fig. 12 Modified Pourbaix diagram for Ce^{4+} and Ce^{3+} soluble species (predominance region for $Ce(OH)_4$ (pt) based on DFT calculation of its free energy; other predominance regions based on previous work[76,150] (pt = amorphous precipitate, s = crystalline solid).

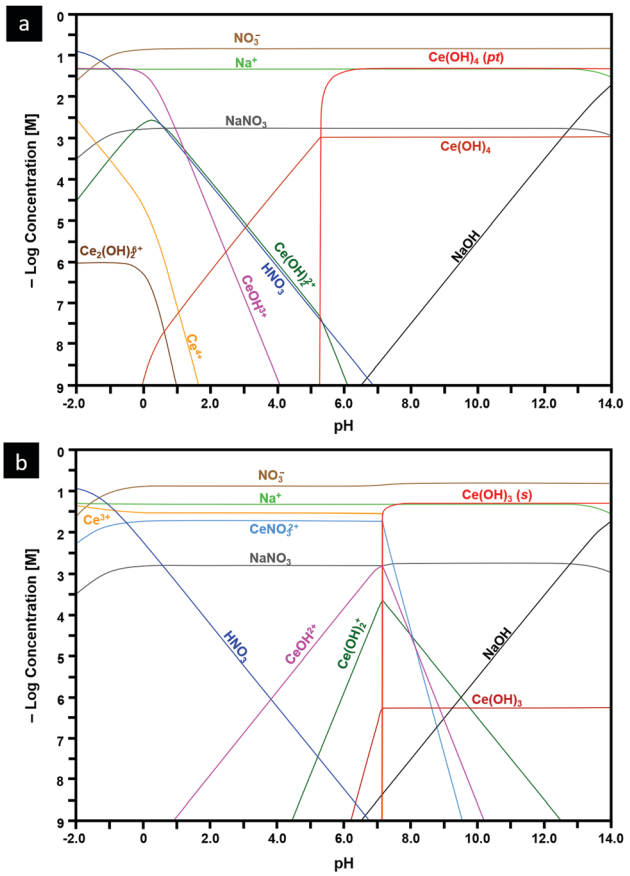

Fig. 13 Speciation diagrams calculated at $[Ce^{4+}]$ and $[Ce^{3+}]$ = 50 mM, $[NO_3^-]$ = 150 mM, $[Na^+]$ = 50 mM for: (a) system Ce^{4+}–H_2O and (b) Ce^{3+}–H_2O (pt = amorphous precipitate, s = crystalline solid).

The formation of solid $Ce(OH)_4$ is supported by earlier versions of this diagram.[76,150] These diagrams also show the formation of solid $Ce(OH)_3$ according to the green predominance region, so $Ce(OH)_3$ could be present as a minor phase at intermediate pH values (~7–11). The specific locations and extents of these predominance regions are unique to each individual chemical system, which explains the possible observation of $Ce(OH)_3$ nanorods.[15,16,80,104,108] Since $Ce(OH)_3$ is considered to oxidise readily to CeO_2,[15,16,80,104,108] this supports by analogy the sequence $Ce(OH)_4$(pt) → CeO_2(s). Differentiation between $Ce(OH)_4$ and $Ce(OH)_3$ is complicated by the relatively easy redox switching between the two Ce valence states.[12,103,104,151] Since the crystal structure of $Ce(OH)_4$ has been reported to be identical to that of cubic CeO_2,[152,153] but that of $Ce(OH)_3$ has been reported to be hexagonal,[16,104] it is possible that these crystal structures reflect the cross sections of the respective nanorods. However, since the present work indicates that cubic $Ce(OH)_4$ can generate both square and hexagonal nanorods, then the only implication is that $Ce(OH)_3$ may be a precursor to hexagonal nanorods.

In conclusion, the preparation of alternative Pourbaix diagrams for different anionic ligands and precipitating agents can illustrate the effects of different chemical species on the sizes and locations of the $Ce(OH)_4$ and $Ce(OH)_3$ predominance regions (in the stability range in water), thereby predicting the potential for the formation of solid $Ce(OH)_4$ or $Ce(OH)_3$ and the required pH conditions.

Fig. 10 also shows the role of the destabilisation of the nanorods (considered to be metastable[16]) by increasing T and/or t). Fig. 8 shows that, unlike the crystallites that comprise the nanochains,[106,110] the crystallites that are liberated by this destabilisation are more rounded and so they exhibit a greater extent of truncation to expose both {110} and {100} planes. These rounded crystallites are subject to subsequent NO_3^- anion selective adsorption on the {100} planes,[15] which facilitates their conversion to cuboidal crystallites that undergo self-assembly, intergrowth, and coalescence into nanocubes. The subsequent growth mechanisms that generate the nanocube variants have been considered by others as well.[15,16,104,113]

Speciation diagrams

The construction of speciation diagrams is an essential preliminary stage to the construction of Pourbaix diagrams.[154,155] Speciation diagrams provide information on the conditions for nonfaradaic chemical reactions of Ce ions, in the absence of oxidation reactions, to form solid $Ce(OH)_4$ (Fig. 13(a) or $Ce(OH)_3$ (Fig. 13(b)). They also define the pH range at which solids will form as well as their concentrations. At a basic level, these diagrams differentiate the aqueous equilibria according to the Ce valence of the precursor salt used for synthesis. In contrast, Pourbaix diagrams include all metal valences and hence incorporate redox reactions. However, Pourbaix diagrams generally consider only the predominant metal-based species of the system while speciation diagrams include all species of the system. The diagrams calculated in the present work are distinctive because they are the first to include data for $Ce(OH)_4$(pt), the Gibbs free energy of which was calculated using DFT.[42] Both speciation diagrams indicate that the concentrations of the anionic ligand NO_3^- are in excess at all pH values. This demonstrates that, for these systems, the concentration of the anionic ligand does not represent a variable that influences the morphological development. In contrast,

the solubility curves for NaOH demonstrate that both the type and concentration of this precipitating agent are variables that do have an impact on the morphological development.

Conclusions

The present work provides an introductory but extensive summary of the fundamental parameters that underpin the design of nanoparticulate morphologies:

- Crystallography
- Optical mineralogy
- Surface plane stabilities
- Stoichiometry
- Phase equilibria
- Thermodynamics
- Defect equilibria
- Crystal growth mechanisms

When these parameters are known and can be controlled and utilised, the designer of nanomaterials, such as CeO_{2-x}, can leverage these to synthesise nanocrystals whose properties have been engineered strategically.

The present work also reports a comprehensive survey of the effects of the key experimental variables [Ce] (and, by association, [NO_3^-]), [NaOH], T (and, by association, P), and t on the morphologies of nanoceria formed during precipitation and hydrothermal synthesis as determined in published reports and the present supplementary experimentation. These data have generated a comprehensive schematic that describes the roles of these variables on the resultant morphologies and the associated mechanisms by which the morphologies are generated, where the variables associated with the types of anionic ligand (NO_3^-) and precipitating agent (NaOH) are fixed.

The present work also clarifies the importance of the formation of nanochains, which are precursors to both square and hexagonal nanorods. The respective mechanisms for the conversion of the nanochains into nanorods have been elucidated crystallographically and reflect a four-stage process of the following:

(1) Anionic ligand bonding between:

– {111} – {111} planes for simple octahedra|square nanorods → zigzag nanochains

– {100} – {100} planes for truncated octahedra|hexagonal nanorods → zigzag nanochains

In the case of truncated octahedra, preferential adsorption of the anionic ligand on the {100} planes to form zigzag nanochains occurs owing to the low stability and polarity of these crystallographic planes.

(2) Condensation and anionic ligand decomposition to establish epitaxy and consolidate the zigzag morphology

(3) Self-assembly and intergrowth to establish pinacoids that form the prism and dipyramid faces

(4) Coalescence and Ostwald ripening to recrystallise single-crystal nanorods

The formation of nanorods is critical to the potential to form nanocubes because the former are precursors to the latter. This conversion process takes place in four or five stages (where Stage 3 may or may not occur), depending on the effects of the anionic ligand on the ultimate morphology:

(1) Disassembly of the nanorods by destabilisation and deterioration

(2) Establishment of rounded crystallites (octahedral spheroids)

(3) NO_3^- selective adsorption or nonadsorption:

– High T: NO_3^- selective adsorption – resultant cube formation

– Low T: nonadsorption – resultant sphere formation

(4) Crystallite self-assembly (cuboids and spheroids)

(5) Crystallite coalescence into established grains

This process effectively includes an unrecognised intermediate stage of crystal growth between those of nucleation and grain establishment.

The apparent uncertainties and contradictions about the crystallographies of the square and hexagonal nanorods have been resolved. These morphologies are not true prismatic nanorods as they do not exhibit true fourfold tetragonal and sixfold hexagonal axial symmetries.

The roles of the anionic ligands have been clarified as well. It is likely that the type and hence the bonding of the anionic ligand are critical to the formation of the nanochains and subsequently their conversion to nanorods. Also, attention has been drawn to the role of NO_3^-, in contrast with other anions, in selective adsorption on {100} in facilitating the conversion of the $Ce(OH)_4$ crystallites, which form upon the destabilisation and deterioration of the nanorods, into nanocubes. Alternatively, when the temperature is too low for the activation of NO_3^- anion selective adsorption on {100}, nanospheres are formed by the process of self-assembly, intergrowth, coalescence, and Ostwald ripening.

A new $Ce^{4+/3+}$–H_2O Pourbaix diagram has been prepared for the predominant Ce-based phases that form in the $Ce^{4+/3+}$–Na^+–NO_3^-–H_2O system. It is distinctive in that it illustrates the importance of the precipitation of amorphous $Ce(OH)_4$, which supports the conclusion that the crystallites that form nanochains and convert to square and hexagonal nanorods originate in $Ce(OH)_4$ crystallites. Other more indicative Pourbaix diagrams for this and alternative systems provide the basis to assess the potential for crystallite and nanoparticle formation as well as the pH ranges suitable to these ends.

Matching new speciation diagrams for the Ce^{4+}–Na^+–NO_3^-–H_2O and Ce^{3+}–Na^+–NO_3^-–H_2O systems also have been prepared. These are the first such diagrams to include the critical data for the amorphous $Ce(OH)_4$ precipitate, which converts readily to the crystalline analogue. Such diagrams of other chemical systems provide the basis for assessing the pH ranges suitable for the exsolution of the $Ce(OH)_4$ and $Ce(OH)_3$ crystallites, which provide the building blocks for the range of morphologies that can form during precipitation and hydrothermal synthesis. Such diagrams are particularly relevant when they indicate the formation of $Ce(OH)_3$(s), which is the basis for a possible CeO_2 nanorod formation pathway not considered in the present work. These diagrams also provide guidance for the selection of precursor salts of different valences, which represent another option open to the researcher seeking to engineer CeO_{2-x} of

specific morphologies. Thus, these diagrams are relevant to the identification of alternative systems that can be used for the synthesis of the range of morphologies open to CeO_{2-x}.

Conflicts of interest

There are no conflicts of interest to declare.

Acknowledgements

The authors acknowledge financial support from the Australian Research Council (ARC), Grant No. DP170104130, and the characterisation facilities provided by the Australian Microscopy & Microanalysis Research Facilities (AMMRF) node at UNSW Sydney.

References

1 J. Kašpar, P. Fornasiero and M. Graziani, *Catal. Today*, 1999, **50**, 285–298.
2 D. Ding, X. Li, S. Y. Lai, K. Gerdes and M. Liu, *Energy Environ. Sci.*, 2014, **7**, 552–575.
3 N. Izu, W. Shin, N. Murayama and S. Kanzaki, *Sens. Actuators, B*, 2002, **87**, 95–98.
4 S. S. Mofarah, E. Adabifiroozjaei, Y. Wang, R. Pardehkhorram, Y. Yao, M. H. N. Assadi, R. Mehmood, W.-F. Chen, C. Tsounis, J. Scott, S. Lim, R. F. Webster, V. Zhong, Y. Xu, P. Koshy and C. C. Sorrell, *J. Mater. Chem. A*, 2020, **8**, 4753–4763.
5 S. S. Mofarah, E. Adabifiroozjaei, R. Pardehkhorram, M. H. N. Assadi, M. Hinterstein, Y. Yao, X. Liu, M. B. Ghasemian, K. Kalantar-Zadeh, R. Mehmood, C. Cazorla, R. Shahmiri, G. Bahmanrokh, S. Bhattacharyya, M. C. Spadaro, J. Arbiol, S. Lim, Y. Xu, H. Arandiyan, J. Scott, P. Koshy and C. C. Sorrell, *Adv. Mater.*, 2019, **31**, 1905288.
6 R. Mehmood, S. S. Mofarah, W.-F. Chen, P. Koshy and C. C. Sorrell, *Inorg. Chem.*, 2019, **58**, 6016–6027.
7 A. Younis, D. Chu and S. Li, *J. Mater. Chem. A*, 2015, **3**, 13970–13977.
8 A. Corma, P. Atienzar, H. Garcia and J.-Y. Chane-Ching, *Nat. Mater.*, 2004, **3**, 394–397.
9 A. Primo, T. Marino, A. Corma, R. Molinari and H. Garcia, *J. Am. Chem. Soc.*, 2011, **133**, 6930–6933.
10 R. Si, Y.-W. Zhang, L.-P. You and C.-H. Yan, *Angew. Chem., Int. Ed.*, 2005, **117**, 3320–3324; *Angew. Chem., Int. Ed.*, 2005, **44**, 3256–3260.
11 I. Celardo, J. Z. Pedersen, E. Traversa and L. Ghibelli, *Nanoscale*, 2011, **3**, 1411–1420.
12 R. Mehmood, X. Wang, P. Koshy, J.-L. Yang and C. C. Sorrell, *CrystEngComm*, 2018, **20**, 1536–1545.
13 A. Estevez and J. S. Erlichman, *Nanomedicine*, 2014, **9**, 1437–1440.
14 R. Mehmood, N. Ariotti, J.-L. Yang, P. Koshy and C. C. Sorrell, *ACS Biomater. Sci. Eng.*, 2018, **4**, 1064–1072.
15 Q. Wu, F. Zhang, P. Xiao and H. Tao, *J. Phys. Chem. C*, 2008, **112**, 17076–17080.
16 T. Sakthivel, S. Das, A. Kumar, D. Reid, A. Gupta, D. Sayle and S. Seal, *ChemPlusChem*, 2013, **78**, 1446–1455.
17 L. Torrente-Murciano, A. Gilbank, B. Puertolas, T. Garcia, B. Solsona and D. Chadwick, *Appl. Catal., B*, 2013, **132**, 116–122.
18 T. Montini, M. Melchionna, M. Monai and P. Fornasiero, *Chem. Rev.*, 2016, **116**, 5987–6041.
19 C. Sun, H. Li and L. Chen, *Energy Environ. Sci.*, 2012, **5**, 8475–8505.
20 A. Trovarelli, *Catal. Rev.*, 1996, **38**, 439–520.
21 *CRC Handbook of Chemistry and Physics*, ed. W. M. Haynes, Taylor & Francis, Boca Raton, FL, 95st edn, 2014, pp. 14–19.
22 J. Wisniak, *Chem. Educator*, 2000, **5**, 343–350.
23 B. T. Kilbourn, *Kirk-Othmer Encyclopedia of Chemical Technology*, Wiley-Interscience, New York, 5th edn, 2004, vol. 5, pp. 670–692.
24 A. B. Goggs, *J. Chem. Soc.*, 1928, 2667–2669.
25 T. Takahashi, K. Ito and H. Iwahara, *Denki Kagaku*, 1966, **34**, 205–209.
26 R. D. Shannon, *Acta Crystallogr., Sect. A: Cryst. Phys., Diffr., Theor. Gen. Crystallogr.*, 1976, **32**, 751–767.
27 R. W. G. Wyckoff, *Crystal Structures*, Wiley-Interscience, New York, 2nd edn, 1963, vol. I, pp. 239–244.
28 C. Cazorla and J. Boronat, *Rev. Mod. Phys.*, 2017, **89**, 035003.
29 Y. Zhang and W. Yang, *J. Chem. Phys.*, 1998, **109**, 2604–2608.
30 S. L. Dudarev, G. A. Botton, S. Y. Savrasov, C. J. Humphreys and A. P. Sutton, *Phys. Rev. B: Condens. Matter Mater. Phys.*, 1998, **57**, 1505–1509.
31 K. Kim and K. D. Jordan, *J. Phys. Chem.*, 1994, **98**, 10089–10094.
32 J. Heyd and G. E. Scuseria, *J. Chem. Phys.*, 2003, **118**, 8207–8215.
33 M. M. Branda, R. M. Ferullo, M. Causà and F. Illas, *J. Phys. Chem. C*, 2011, **115**, 3716–3721.
34 Y. Jiang, J. B. Adams and M. van Shilfgaarde, *J. Chem. Phys.*, 2005, **123**, 064701.
35 C. Noguera, *Surf. Rev. Lett.*, 2001, **8**, 121–167.
36 J. C. Conesa, *Surf. Sci.*, 1995, **339**, 337–352.
37 I. Riess, H. Janczikowski and J. Nölting, *J. Appl. Phys.*, 1987, **61**, 4931–4933.
38 M. Hillert and B. Jansson, *J. Am. Ceram. Soc.*, 1986, **69**, 732–734.
39 H. L. Tuller and A. S. Nowick, *J. Electrochem. Soc.*, 1979, **126**, 209–217.
40 B. Bulfin, A. J. Lowe, K. A. Keogh, B. E. Murphy, O. Lübben, S. A. Krasnikov and I. V. Shvets, *J. Phys. Chem. C*, 2013, **117**, 24129–24137.
41 R. G. Schwab, R. A. Steiner, G. Mages and H.-J. Beie, *Thin Solid Films*, 1992, **207**, 288–293.
42 S. S. Mofarah, E. Adabifiroozjaei, Y. Yao, P. Koshy, S. Lim, R. Webster, X. Liu, R. K. Nekouei, C. Cazorla, Z. Liu, Y. Wang, N. Lambropoulos and C. C. Sorrell, *Nat. Commun.*, 2019, **10**, 2594.
43 H. Okamoto, *J. Phase Equil. Diff.*, 2008, **29**, 545–547.
44 S. Andersson, B. Collén, U. Kuylenstierna and A. Magnéli, *Acta Chem. Scand.*, 1957, **11**, 1641–1652.
45 F. Wang, R. Shi, Y. Lei, Z. Lei, R. Jiang, D. Wang, Z. Liu and J. Sun, *CrystEngComm*, 2019, **21**, 524–534.

46 S. Harada, K. Tanaka and H. Inui, *J. Appl. Phys.*, 2010, **108**, 083703.
47 A. F. Arif, R. Balgis, T. Ogi, F. Iskandar, A. Konoshita, K. Nakamura and K. Okuyama, *Sci. Rep.*, 2017, **7**, 3646.
48 A. C. M. Padilha, H. Raebiger, A. R. Rocha and G. M. Dalpian, *Sci. Rep.*, 2016, **6**, 28871.
49 I. Slipukhina and M. Ležaić, *Phys. Rev. B: Condens. Matter Mater. Phys.*, 2014, **90**, 155133.
50 M. N. Gordos, *Tribol. Lett.*, 2000, **8**, 65–78.
51 J. E. Wertz, in *Mass Transport in Oxides*, ed. J. B. Wachtman Jr. and A. D. Franklin, National Bureau of Standards, Washington, D.C., 1968, pp. 11–23.
52 F. A. Kröger and H. J. Vink, in *Solid State Physics*, ed. F. Seitz and D. Turnbull, Elsevier, City, 1956, vol. 3, pp. 307–435.
53 A. Migani, G. N. Vayssilov, S. T. Bromley, F. Illas and K. M. Neyman, *Chem. Commun.*, 2010, **46**, 5936–5938.
54 H.-F. Wang, H.-Y. Li, X.-Q. Gong, Y.-L. Guo, G.-Z. Lu and P. Hu, *Phys. Chem. Chem. Phys.*, 2012, **14**, 16521–16535.
55 T. Close, G. Tulsyan, C. A. Diaz, S. J. Weinstein and C. Richter, *Nat. Nanotechnol.*, 2015, **10**, 418–422.
56 G. Bahmanrokh, C. Cazorla, S. S. Mofarah, R. Shahmiri, Y. Yao, I. Ismail, W.-F. Chen, P. Koshy and C. C. Sorrell, *Nanoscale*, 2020, **12**, 4916–4934.
57 V. Kumar, W.-F. Chen, X. Zhang, Y. Jiang, P. Koshy and C. C. Sorrell, *Ceram. Int.*, 2019, **45**, 22085–22094.
58 Z. Liu, W.-F. Chen, X. Zhang, J. Zhang, P. Koshy and C. C. Sorrell, *J. Phys. Chem. C*, 2019, **123**, 11781–11790.
59 Y. Jiang, W.-F. Chen, P. Koshy and C. C. Sorrell, *J. Mater. Sci.*, 2019, **54**, 5266–5279.
60 D. Mittal, W.-F. Chen, P. Koshy, H.-K. Chen, I. Kabir, Y. Jiang, Z. Liu and C. C. Sorrell, *SN Appl. Sci.*, 2019, **1**, 234.
61 Y. Cui, W.-F. Chen, A. Bastide, X. Zhang, P. Koshy and C. C. Sorrell, *J. Phys. Chem. Solids*, 2019, **126**, 314–321.
62 W.-F. Chen, S. S. Mofarah, D. A. H. Hanaor, P. Koshy, H.-K. Chen, Y. Jiang and C. C. Sorrell, *Inorg. Chem.*, 2018, **57**, 7279–7289.
63 W.-F. Chen, H. Chen, P. Koshy, A. Nakaruk and C. C. Sorrell, *Mater. Chem. Phys.*, 2018, **205**, 334–346.
64 H. Ren, J. Wang, H. Ma, F. Cao, Y. Jiang, P. Koshy and C. C. Sorrell, *New J. Chem.*, 2018, **42**, 19685–19691.
65 W.-F. Chen, P. Koshy, L. Adler and C. C. Sorrell, *J. Austral. Ceram. Soc.*, 2017, **53**, 569–576.
66 L. Chung, W.-F. Chen, P. Koshy and C. C. Sorrell, *Mater. Chem. Phys.*, 2017, **197**, 236–239.
67 W.-F. Chen, P. Koshy, Y. Huang, E. Adabifiroozjaei, Y. Yao and C. C. Sorrell, *Int. J. Hydrogen Energy*, 2016, **41**, 19025–19056.
68 H. Ren, P. Koshy, F. Cao and C. C. Sorrell, *Inorg. Chem.*, 2016, **55**, 8071–8081.
69 W.-F. Chen, P. Koshy and C. C. Sorrell, *Int. J. Hydrogen Energy*, 2015, **40**, 16215–16229.
70 L. R. Shah, B. Ali, H. Zhu, W. G. Wang, Y. Q. Song, H. W. Zhang, S. I. Shah and J. Q. Xiao, *J. Phys.: Condens. Matter*, 2009, **21**, 486004.
71 S. Aškrabić, Z. D. Dohčević-Mitrović, V. D. Araújo, G. Ionita, M. M. de Lima Jr. and A. Cantarero, *J. Phys. D: Appl. Phys.*, 2013, **46**, 495306.
72 J.-M. Costantini, G. Lelong, M. Guillaumet, W. J. Weber, S. Takaki and K. Yasuda, *J. Phys.: Condens. Matter*, 2016, **28**, 325001.
73 S. Soni, S. Kumar, R. S. Meena, V. S. Vats and S. Dalela, *AIP Conf. Proc.*, 2015, **1665**, 130029.
74 Q.-Y. Wen, H.-W. Zhang, Y.-Q. Song, Q.-H. Yang, H. Zhu and J. Q. Xiao, *J. Phys.: Condens. Matter*, 2007, **19**, 246205.
75 S.-Y. Chen, C.-H. Tsai, M.-Z. Huang, D.-C. Yan, T.-W. Huang, A. Gloter, C.-L. Chen, H.-J. Lin, C.-T. Chen and C.-L. Dong, *J. Phys. Chem. C*, 2012, **116**, 8707–8713.
76 D. Channei, S. Phanichphant, A. Nakaruk, S. S. Mofarah, P. Koshy and C. C. Sorrell, *Catalysts*, 2017, **7**, 45.
77 E. Tani, M. Yoshimura and S. Sōmiya, *J. Mater. Sci. Lett.*, 1982, **1**, 461–462.
78 M. Hirano and E. Kato, *J. Am. Ceram. Soc.*, 1996, **79**, 777–780.
79 G.-S. Li, S.-H. Feng and L.-P. Li, *J. Solid State Chem.*, 1996, **126**, 74–79.
80 K. Zhou, Z. Yang and S. Yang, *Chem. Mater.*, 2007, **19**, 1215–1217.
81 X. Q. Fu, C. Wang, H. C. Yu, Y. G. Wang and T. H. Wang, *Nanotechnology*, 2007, **18**, 145503.
82 C. Tang, Y. Bando, B. Liu and D. Golberg, *Adv. Mater.*, 2005, **17**, 3005–3009.
83 N.-C. Wu, E.-W. Shi, Y.-Q. Zheng and W.-J. Li, *J. Am. Ceram. Soc.*, 2002, **85**, 2462–2468.
84 W. Wang, J. Y. Howe, Y. A. Li, X. F. Qiu, D. C. Joy, M. P. Paranthaman, M. J. Doktycz and B. H. Gu, *J. Mater. Chem.*, 2010, **20**, 7776–7781.
85 Z. Yang, J. Wei, H. Yang, K. Liu, H. Liang and Y. Yang, *Eur. J. Inorg. Chem.*, 2010, 3354–3359.
86 A. Vantomme, Z.-Y. Yuan, G. Du and B.-L. Su, *Langmuir*, 2005, **21**, 1132–1135.
87 C. Sun, H. Li, Z. X. Wang, L. Chen and X. Huang, *Chem. Lett.*, 2004, **33**, 662–663.
88 C. Laberty-Robert, J. W. Long, E. M. Lucas, K. A. Pettigrew, R. M. Stroud, M. S. Doescher and D. R. Rolison, *Chem. Mater.*, 2006, **18**, 50–58.
89 Z. Ji, X. Wang, H. Zhang, S. Lin, H. Meng, B. Sun, S. George, T. Xia, A. E. Nel and J. I. Zink, *ACS Nano*, 2012, **6**, 5366–5380.
90 C. Sun, H. Li, H. Zhang, Z. Wang and L. Chen, *Nanotechnology*, 2005, **16**, 1454–1463.
91 L. Yan, X. Xing, R. Yu, J. Deng, J. Chen and G. Liu, *Phys. B*, 2007, **390**, 59–64.
92 M. Hirano and M. Inagaki, *J. Mater. Chem.*, 2000, **10**, 473–477.
93 H.-L. Lin, C.-Y. Wu and R.-K. Chiang, *J. Colloid Interface Sci.*, 2010, **341**, 12–17.
94 W.-Q. Han, L. Wu and Y. Zhu, *J. Am. Chem. Soc.*, 2005, **127**, 12814–12815.
95 H.-L. Lin, C.-Y. Wu and R.-K. Chiang, *J. Colloid Interface Sci.*, 2010, **341**, 12–17.
96 T. Yu, B. Lim and Y. Xia, *Angew. Chem., Int. Ed.*, 2010, **122**, 4586–4589; *Angew. Chem. Int. Ed.*, 2010, **49**, 4484-4487.
97 R. Yu, L. Yan, P. Zheng, J. Chen and X. Xing, *J. Phys. Chem. C*, 2008, **112**, 19896–19900.

98 B. Tang, L. Zhuo, J. Ge, G. Wang, Z. Shi and J. Niu, *Chem. Commun.*, 2005, 3565–3567.
99 P. Wang and K. Kobiro, *Pure Appl. Chem.*, 2014, **86**, 785–800.
100 Y. Zhang, T. Cheng, Q. Hu, Z. Fang and K. Han, *J. Mater. Res.*, 2007, **22**, 1472–1478.
101 W. Wang, J. Y. Howe, Y. Li, X. Qiu, D. C. Joy, M. P. Paranthaman, M. J. Doktycz and B. Gu, *J. Mater. Chem.*, 2010, **20**, 7776–7781.
102 Anonymous, *Solid – Liquid Equilibrium (SLE) and Vapour – Liquid Equilibrium (VLE) of Aqueous NaOH* (M. Conde Engineering, Zurich, Switzerland, June 2014).
103 A. Trovarelli and J. Llorca, *ACS Catal.*, 2017, **7**, 4716–4735.
104 H.-X. Mai, L.-D. Sun, Y.-W. Zhang, R. Si, W. Feng, H.-P. Zhang, H.-C. Liu and C.-H. Yan, *J. Phys. Chem. B*, 2005, **109**, 24380–24385.
105 K. Zhou, X. Wang, X. M. Sun, Q. Peng and Y. Li, *J. Catal.*, 2005, **229**, 206–212.
106 N. Du, H. Zhang, B.-D. Chen, X.-Y. Ma and D.-R. Yang, *J. Phys. Chem. C*, 2007, **111**, 12677–12680.
107 Z. Liu, X.-J. Li, M. Mayyas, P. Koshy, J. N. Hart and C. C. Sorrell, *CrystEngComm*, 2017, **19**, 4766–4776.
108 C. Pan, D. Zhang, L. Shi and J. Fang, *Eur. J. Inorg. Chem.*, 2008, 2429–2436.
109 M. Nabavi, O. Spalla and B. Cabane, *J. Colloid Interface Sci.*, 1993, **160**, 459–471.
110 L. Agarwal, B. Lefferts, D. Mojet, E. D. Ligthart, D. Hensen, W. Mitchell, B. Erasmus, E. Anderson, J. Olivier, J. Neethling and A. Datye, *ChemSusChem*, 2013, **6**, 1898–1906.
111 T. S. Sakthivel, D. L. Reid, U. M. Bhatta, G. Möbus, D. C. Sayle and S. Seal, *Nanoscale*, 2015, **7**, 5169–5177.
112 Q. Yuan, H.-H. Duan, L.-L. Li, L.-D. Sun, Y.-W. Zhang and C.-H. Yan, *J. Colloid Interface Sci.*, 2009, **335**, 151–167.
113 S.-W. Yang and L. Gao, *J. Am. Chem. Soc.*, 2006, **128**, 9330–9331.
114 Y. Kamimura, M. Shimomura and A. Endo, *J. Colloid Interface Sci.*, 2014, **436**, 52–62.
115 M. Lin, Z. Y. Fu, H. R. Tan, J. P. Y. Tan, S. C. Ng and E. Teo, *Cryst. Growth Des.*, 2012, **12**, 3296–3303.
116 M. Lykaki, E. Pachatouridou, E. Iliopoulou, S. A. C. Carabineiro and M. Konsolakis, *RSC Adv.*, 2017, **7**, 6160–6169.
117 X. Guo and R. Zhou, *J. Power Sources*, 2017, **361**, 39–53.
118 J. Li, Z.-Y. Zhang, Z.-M. Tian, X.-M. Zhou, Z.-P. Zheng, Y.-Y. Ma and Y.-Q. Qu, *J. Mater. Chem. A*, 2014, **2**, 16459–16466.
119 Z.-L. Wu, M.-J. Li, J. Howe, H. M. Meyer and S. H. Overbury, *Langmuir*, 2010, **26**, 16595–16606.
120 Y.-J. Liu, Z.-F. Li, H.-B. Xu and Y.-Y. Han, *Catal. Commun.*, 2016, **76**, 1–6.
121 U. M. Bhatta, D. Reid, T. Sakthivel, T. X. T. Sayle, D. Sayle, M. Molinari, S. C. Parker, I. M. Ross, S. Seal and G. Möbus, *J. Phys. Chem. C*, 2013, **117**, 24561–24569.
122 C. Lei, A. Rockett and I. M. Robertson, *J. Appl. Phys.*, 2006, **100**, 073518.
123 K. H. Hansen, T. Worren, S. Stempel, E. Lægsgaard, M. Bäumer, H.-J. Freund, F. Besenbacher and I. Stensgaard, *Phys. Rev. Lett.*, 1999, **83**, 4120–4123.
124 J. E. Prieto and I. Markov, *Europhys. Lett.*, 2014, **108**, 46007.
125 X.-D. Feng, D. C. Sayle, Z.-L. Wang, M. S. Paras, B. Santora, A. C. Sutorik, T. X. T. Sayle, Y. Yang, Y. Ding, X.-D. Wang and Y.-S. Her, *Science*, 2006, **312**, 1504–1508.
126 J. W. Mullin, *Crystallization*, Butterworth-Heinemann, London, 3rd edn, 1997, pp. 172–260.
127 Z. Ji, X. Wang, H. Zhang, S. Lin, H. Meng, B. Sun, S. George, T. Xia, A. E. Nel and J. I. Zink, *ACS Nano*, 2012, **6**, 5366–5380.
128 D.-S. Li, M. H. Nielsen, J. R. I. Lee, C. Frandsen, J. F. Banfield and J. J. D. Yoreo, *Science*, 2012, **336**, 1014–1018.
129 V. K. Ivanov, P. P. Fedorov, A. Y. Baranchikov and V. V. Osiko, *Russ. Chem. Rev.*, 2014, **83**, 1204–1222.
130 J. Zhang, F. Huang and Z. Lin, *Nanoscale*, 2010, **2**, 18–34.
131 S. Wang, L. Zhao, W. Wang, Y. Zhao, G. Zhang, X. Ma and J. Gong, *Nanoscale*, 2013, **5**, 5582–5588.
132 G. Spezzati, A. D. Benavidez, A. T. DeLaRiva, Y. Su, J. P. Hofmann, S. Asahina, E. J. Olivier, J. H. Neething, J. T. Miller, A. K. Datye and E. J. M. Hensen, *Appl. Catal., B*, 2019, **243**, 36–46.
133 A. Röckert, J. Kullgren, P. Broqvist, S. Alwan and K. Hermansson, *J. Chem. Phys.*, 2020, **152**, 104709.
134 M. Nolan, S. C. Parker and G. W. Watson, *Surf. Sci.*, 2005, **595**, 223–232.
135 Y. Pan, N. Nilius, C. Stiehler, H.-J. Freund, J. Goniakowski and C. Noguera, *Interfaces*, 2014, **1**, 1400404.
136 J. Huang, Y. Yu, J. Zhu and R. Yu, *Sci. China Mater.*, 2017, **60**, 903–908.
137 Y. Lin, Z. Wu, J. Wen, K. Ding, X. Yang, K. R. Poeppelmeier and L. D. Marks, *Nano Lett.*, 2015, **15**, 5375–5381.
138 M. S. A. Asghar, B. J. Inkson and G. Möbus, *J. Mater. Sci.*, 2020, **55**, 2815–2825.
139 S. K. Kannan and M. Sundrarajan, *Int. J. Nanosci.*, 2014, **13**, 1450018.
140 R. Rao, M. Yang, Q. Ling, Q. Zhang, H. Liu, A. Zhang and W. Chen, *Microporous Mesoporous Mater.*, 2013, **169**, 81–87.
141 M. Zarinkamar, M. Farahmandjou and T. P. Firoozabadi, *Ceram. Proc. Res.*, 2016, **17**, 166–169.
142 R. Schmitt, A. Nenning, O. Kraynis, R. Korobko, A. I. Frenkel, I. Lubomirsky, S. M. Haile and J. L. M. Rupp, *Chem. Soc. Rev.*, 2020, **49**, 554–592.
143 C. Sun, H. Li and L. Chen, *Energy Environ. Sci.*, 2012, **5**, 8475–8505.
144 A. Trovarelli, *Catal. Rev.*, 1996, **38**, 439–520.
145 Y. Lin, Z. Wu, J. Wen, K. R. Poeppelmeier and L. D. Marks, *Nano Lett.*, 2013, **14**, 191–196.
146 W.-X. Tang and P.-X. Gao, *MRS Commun.*, 2016, **6**, 311–329.
147 L. Yan, R. Yu, J. Chen and X. Xing, *Cryst. Growth Des.*, 2008, **8**, 1474–1477.
148 B. Liu, M. Yao, B. Liu, Z. Li, R. Liu, Q. Li, D. Li, B. Zou, T. Cui and G. Zou, *J. Phys. Chem. C*, 2011, **115**, 4546–4551.
149 D. Zhang, X. Du, L. Shi and R. Gao, *Dalton Trans.*, 2012, **41**, 14455–14475.
150 S. A. Hayes, P. Yu, T. J. O'Keefe, M. J. O'Keefe and J. O. Stoffer, *J. Electrochem. Soc.*, 2002, **149**, 623–630.

151 T. V. Plakhova, A. Y. Romanchuk, S. N. Yakunin, T. Dumas, S. Demir, S. Wang, S. G. Minasian, D. K. Shuh, T. Tyliszczak, A. A. Shiryaev, A. V. Egorov, V. K. Ivanov and S. N. Kalmykov, *J. Phys. Chem. C*, 2016, **120**, 22615–22626.
152 P. Abellan, T. H. Moser, I. T. Lucas, J. W. Grate, J. E. Evans and N. D. Browning, *RSC Adv.*, 2017, **7**, 3831–3837.
153 A. A. Ansari and A. Kaushik, *J. Semicond.*, 2010, **31**, 033001.
154 S. Fränzle, B. Markert and S. Wünschmann, *Introduction to Environmental Engineering*, Wiley-VCH, Weinheim, Germany, 2012, pp. 212–225.
155 E. D. Verink, Jr., in *Uhlig's Corrosion Handbook*, ed. R. W. Revie, John Wiley, New York, 3rd edn, 2011, pp. 93–101.